Embedding a One-column Ocean Model (SIT 1.06) in the Community Atmosphere Model 5.3 (CAM5.3; CAM5–SIT v1.0) to Improve Madden–Julian Oscillation Simulation in Boreal Winter

Yung-Yao Lan, Huang-Hsiung Hsu[*], Wan-Ling Tseng, and Li-Chiang Jiang

Research Center for Environmental Changes, Academia Sinica, Taipei 11529, Taiwan

[*]*Correspondence to*: Huang-Hsiung Hsu (hhhsu@gate.sinica.edu.tw)

10 **Abstract**

11   The effect of the air–sea interaction on the Madden–Julian Oscillation (MJO)

12 was investigated using the one-column ocean model Snow–Ice–Thermocline (SIT

13 1.06) embedded in the Community Atmosphere Model 5.3 (CAM5.3; hereafter

14 CAM5–SIT v1.0). The SIT model with 41 vertical layers was developed to simulate

15 sea surface temperature (SST) and upper-ocean temperature variations with a high

16 vertical resolution that resolves the cool skin and diurnal warm layer and the upper

17 oceanic temperature gradient. A series of 30-year sensitivity experiments were

18 conducted in which various model configurations (e.g., coupled versus uncoupled,

19 vertical resolution and depth of the SIT model, coupling domains, and absence of the

20 diurnal cycle) were considered to evaluate the effect of air–sea coupling on MJO

21 simulation. Most of the CAM5–SIT experiments exhibit higher fidelity than the

22 CAM5-alone experiment in characterizing the basic features of the MJO such as

23 spatiotemporal variability and the eastward propagation in boreal winter. The overall

24 MJO simulation performance of CAM5–SIT benefits from (1) better resolving the

25 fine vertical structure of upper-ocean temperature and therefore the air–sea interaction

26 that result in more realistic intraseasonal variability in both SST and atmospheric

27 circulation and (2) the adequate thickness of a vertically-gridded ocean layer. The

28 sensitivity experiments demonstrate the necessity of coupling the tropical eastern

29 Pacific in addition to the tropical Indian Ocean and the tropical western Pacific.

30 Coupling is more essential in the south than north of the equator in the tropical

31 western Pacific. Enhanced MJO could be obtained without considering the diurnal

32 cycle in coupling.

1. Introduction

The Madden–Julian Oscillation (MJO) is a tropical large-scale convection circulation system that propagates eastward across the warm pool region from the tropical Indian Ocean (IO) to the western Pacific (WP) on an intraseasonal time scale (Madden and Julian, 1972). The MJO is not just an atmospheric phenomenon. The findings from a multi-nation field campaign in the tropics called the Dynamics of MJO/Cooperative Indian Ocean Experiment on Intraseasonal Variability in the Year 2011 (DYNAMO/CINDY2011; de Szoeke et al., 2017; Johnson and Ciesielski, 2017; Pujiana et al., 2018; Yoneyama et al., 2013; Zhang and Yoneyama, 2017) revealed vigorous air–sea coupling during the evolution of the MJO (Chang et al., 2019; DeMott et al., 2015; Jiang et al., 2015, 2020; Kim et al., 2010; Li et al., 2016; Li et al., 2020; Newman et al., 2009; Pei et al., 2018; Tseng et al., 2014). During the suppression of convection, the MJO propagates eastward with light winds, which is accompanied by enhanced downwelling shortwave radiation absorption, weaker upward latent and sensible fluxes, less cloudiness and precipitation, and weaker vertically turbulent mixing in the upper ocean, thus causing an increase in the upper-ocean temperature. In the following active phase when deep convection occurs, downwelling shortwave radiation is reduced and stronger westerly winds enhance latent/sensible heat flux (LHF/SHF) loss from the ocean surface, thus causing a decrease in the upper-ocean temperature (DeMott et al., 2015; Madden and Julian, 1972, 1994; Zhang, 2005).

In addition to the tropical ocean surface, the structure of the upper ocean also evolves. Alappattu et al. (2017) reported that during an MJO event, surface flux perturbations cause changes in the ocean thermohaline structure, thus affecting the mixed-layer temperature. The following change in sea surface temperature (SST) can further affect atmospheric circulation of the MJO. Variations in SST mediate LHF and

59   SHF exchange across the air–sea interface. Although SST responds to atmospheric

60   forcing, the modulation of LHF and SHF provides feedback to the atmosphere

61   (DeMott et al., 2015; Jiang et al., 2020). Li et al. (2008, 2020) proposed that the phase

62   relationship between SST and convection implies a delayed air–sea interaction

63   mechanism whereby a preceding active-phase MJO may trigger an inactive-phase

64   MJO through the delayed effect of the induced SST anomaly over the IO. The

65   reduction in SST caused by a preceding active-phase MJO may, in turn, yield delayed

66   ocean feedback that initiates a suppressed-phase MJO, and vice versa. The by-no-

67   means negligible effect of intraseasonal SST variations caused by surface heat fluxes

68   suggests that the ocean state can affect the MJO (DeMott et al., 2015, 2019; Hong et

69   al., 2017; Li et al., 2020).

70   Since its discovery almost five decades ago, the MJO remains a phenomenon

71   that poses a challenge to the capacity of state-of-the-art atmospheric general

72   circulation models (AGCMs) such as those participating in the Coupled Model

73   Intercomparison Project phase 5 and 6 to generate successful simulations (Ahn et al.,

74   2017, 2020; Bui and Maloney 2018; Jiang et al., 2020; Hung et al., 2013; Kim et al.,

75   2011).

76   Recent studies have reported that air–sea coupling improves the representation of

77   the MJO in numerical simulation (Bernie et al., 2008; Crueger et al., 2013; DeMott et

78   al., 2015; Li et al., 2016; Li et al., 2020; Tseng et al., 2014; Woolnough et al., 2007).

79   Tseng et al. (2014) indicated that effectively resolving the tropical upper-ocean warm

80   layer to capture temperature variations in the upper few meters of the ocean could

81   improve MJO simulation. DeMott et al. (2015) suggested that the tropical

82   atmosphere–ocean interaction may sustain or amplify the pattern of the enhanced and

83   suppressed atmospheric convection of the eastward propagation. DeMott et al. (2019)

84   demonstrated that the improved MJO eastward propagation in four coupled models

4

85   resulted from enhanced low-level convective moistening for a rainfall rate of >5 mm

86   day^{-1} due to air–sea coupling. In addition, numerical experiments have been

87   performed to investigate the effect of the diurnal cycle on the MJO (Hagos et al.,

88   2016; Oh et al., 2013), with the results suggesting that the strength and propagation of

89   the MJO through the Maritime Continent (MC) were enhanced when the diurnal cycle

90   was ignored.

91   Although previous studies have demonstrated the importance of considering the

92   air–sea interaction in a numerical model to improve MJO simulation, additional

93   details regarding model configuration (e.g., vertical resolution and total depth of the

94   vertically-gridded ocean, coupling domain, and absence of the diurnal cycle in air–sea

95   coupling) have not been systematically explored. Tseng et al. (2014) coupled the one-

96   column ocean model Snow–Ice–Thermocline (SIT; Tu and Tsuang, 2005) to the fifth

97   generation of the ECHAM AGCM (ECHAM5–SIT) in the tropics and indicated that a

98   vertical resolution of 1 m was essential to yield an improved simulation of the MJO

99   with a realistic strength and eastward propagation speed.

100   In this study, we coupled the SIT model to the Community Atmosphere Model

101   version 5.3 (CAM5.3; Neale et al., 2012)—the atmosphere component of the

102   Community Earth System Model version 1.2.2 (CESM1.2.2; Hurrell et al., 2013) —to

103   explore the improvement of MJO simulation by coupling SIT model to another

104   AGCM is reproducible in modeling science. The CAM5.3, which has been widely

105   used for the long-term simulation of the climate system, could not efficiently simulate

106   the eastward propagation of the MJO; instead, the model simulated a tendency for the

107   MJO to move westward in the IO (Boyle et al., 2015, Jiang et al, 2015). By contrast,

108   the updated CESM2 with the new CAM6 could realistically simulate the MJO (Ahn et

109   al., 2020; Danabasoglu et al., 2020). Thus, the well-explored CAM5, which does not

110   produce a realistic MJO, appears to be a favorable choice for exploring coupling a

111   simple one-dimensional (1-D) ocean model over the tropical oceans, such as the SIT

112   model, can improve MJO simulation, as well as the effects of model configuration on

113   the degree of the improvement. Such a study can also enhance our understanding

114   regarding the effect of air–sea coupling on the MJO.

115   The MJO is a tropical atmosphere system that exhibits a more substantial

116   eastward propagation in boreal winter than in other seasons was the targeted feature in

117   this study. To examine the sensitivity of MJO simulations to different configurations

118   of the tropical air–sea coupling, we conducted a series of 30-year numerical

119   experiments by considering various model configurations (e.g., coupled versus

120   uncoupled, vertical resolution and depth of the SIT model, coupling domains, and

121   absence of the diurnal cycle) to investigate the effect of air–sea coupling. This paper

122   is organized as follows. Section 2 describes the data for validation, the model used for

123   simulation, and the design of numerical experiments. Section 3 describes the effect of

124   various tropical air–sea coupling configurations on the MJO simulation determined

125   through detailed MJO diagnostics. Discussion and conclusions are provided in

126   Section 4.

127

128   **2. Data, methodology, model description, and experimental designs**

129   **2.1 Data and methodology**

130   The data analyzed in this study include precipitation from the Global

131   Precipitation Climatology Project (GPCP), outgoing longwave radiation (OLR) and

132   daily SST (Optimum Interpolation SST; OISST) from the National Oceanic and

133   Atmosphere Administration (NOAA), and parameters from the ERA-Interim (ERA-I)

134   reanalysis (Adler et al., 2003; Dee et al., 2011; Lee et al., 2011; Reynolds and Smith,

135   1995; Schreck et al., 2018). The SST data for the SIT model were obtained from the

136   Hadley Centre Sea Ice and Sea Surface Temperature dataset (Rayner et al., 2003;

137   HadISST1) and the ocean subsurface data (40-layer climatological ocean temperature,

138   salinity, and currents) for nudging were retrieved from the National Centers for

139   Environmental Prediction (NCEP) Global Ocean Data Assimilation System (GODAS;

140   Behringer and Xue, 2004).

141   We used the CLIVAR MJO Working Group diagnostics package (CLIVAR,

142   2009) and a 20–100-day filter (Kaylor, 1977; Wang et al., 2014) to determine

143   intraseasonal variability. MJO phases were defined following the index (namely,

144   RMM1 and RMM2) proposed by Wheeler and Hendon (2004), which considered the

145   first two principal components of the combined near-equatorial OLR and zonal winds

146   at 850 and 200 hPa. The band-passed filtered data were used for calculating the index

147   and defining phases.

148

149   **2.2 Model description**

150   **2.2.1 CAM5.3**

151   The CAM5.3 used in this study has a horizontal resolution of 1.9° latitude ×

152   2.5° longitude and 30 vertical levels with the model top at 0.1 hPa. The MJO could

153   not be realistically simulated in the CAM5.3. Boyle et al. (2015) demonstrated that

154   although making the deep convection dependent on SST improved the simulation of

155   the MJO variance, it exerted a significant negative effect on the mean-state climate of

156   low-level cloud and absorbed shortwave radiation. By comparing the simulation

157   results of an uncoupled and coupled CAM5.3, Li et al. (2016) suggested that air–sea

158   coupling and the convection scheme most significantly affected the MJO simulation

159   in the climate model.

160

161   **2.2.2 1-D high-resolution TKE ocean model**

162   The 1-D high-resolution turbulence kinetic energy (TKE) ocean model SIT was

163   used to simulate the diurnal fluctuation of SST and surface energy fluxes (Lan et al.,

164   2010; Tseng et al., 2014; Tu and Tsuang, 2005). A description of the 1-D high-

165   resolution ocean model SIT can be found in the appendix. The model was well

166   verified against in situ measurements on board the R/V Oceanographic Research

167   Vessel 1 and 3 over the South China Sea (Lan et al., 2010) and on R/V Vickers over

168   the tropical WP (Tu and Tsuang, 2005).

169   The SIT model determines the vertical profiles of the temperature and

170   momentum of a water column from the surface down to the seabed, except in the

171   fixed ocean model bottom experiment. The default setting of vertical discretization

172   (e.g., in the control coupled experiment) is 41 layers with 12 layers in the first 10.5 m,

173   6 layers between 10.5 m and 107.8 m (appendix Fig. A1). In the 1-D TKE ocean

174   model, temperature and salinity below 107.8 m, where vertical turbulent mixing is

175   greatly weakened, are nudged toward the climatological values of GODAS data until

176   4607 m. The extra high vertical resolution is needed to catch detailed temporal

177   variation of upper ocean temperature characterized by the warm layer and cool skin

178   (Tu and Tsuang, 2005). To account for the neglected horizontal advection heat flux,

179   the ocean is weakly nudged (by using a 30-day time scale) between 10.5 m and 107.8

180   m and strongly nudged (by using a 1-day time scale) below 107.8 m according to the

181   NCEP GODAS climatological ocean temperature. No nudging is performed within

182   the upper-most 10.5 m. The SIT model calculates twice for each CAM5 time step (30

183   min; i.e., coupling 48 times per day).

184

185   **2.3 Experimental design**

186   A series of 30-year numerical experiments (Table 1) were conducted to

187   investigate the effect of the air–sea interaction on the MJO simulation. The HadSST1

188   used to force the coupled and uncoupled model was the climatological monthly-mean

189   SST averaged over 1982-2001. The monthly SST was linearly interpolated to daily

190   SST fluctuation that forced the model. The SST in the air–sea coupling tropical

191   region was recalculated by the SIT during the simulation, while the prescribed annual

192   cycle of SST was used in the areas outside the coupling region. Ocean bathymetry of

193   the SIT was derived from the NOAA ETOPO1 data (Amante and Eakins, 2009) and

194   interpolated into $1.9° \times 2.5°$ horizontal resolution.

195   All simulations were driven by the prescribed annual cycle of SST repeatedly for

196   30 years. The strategy is to evaluate the simulation capacity of climate models under

197   the same condition without considering interannual variation induced by SST. This

198   approach has been widely adopted in many studies (Delworth et al., 2006; Haertel et

199   al., 2020; Subramanian et al., 2011; Tseng et al., 2014; Wang et al., 2005).

200   Atmospheric initial conditions and external forcing such as CO_2, ozone, and

201   aerosol in near-equilibrium climate state around the year 2000 were taken from

202   F_2000_CAM5 component set based on CESM1.2.2 framework development. The

203   data has been commonly used in present-day simulations using CAM5 (e.g., He et al.,

204   2017).

205   The setup of five sets of experiment conducted in this study are described as

206   follows.

207   (1) A standalone CAM5.3 simulation forced by climatological monthly HadISST1

208   (A–CTL) and the control experiment of coupled CAM5–SIT simulation (C–

209   30NS; 41 vertical levels, coupling in the entire tropics between 30°N and 30°S

210   with a diurnal cycle). The reasons for tropical coupling are two folds.

211   Considering that the MJO is essentially a tropical phenomenon, the coupling was

212   implemented only between 30°N and 30°S. Secondly, coupling a one-

213   dimensional ocean model in the extratropics without surface flux correction as in

214   our case would ignore the impacts of strong ocean currents (such as the Kuroshio

215   and Gulf Stream) and result in large biases.

216   (2) Upper-ocean vertical resolution experiment: Two simulations with the first layer

217   centering at 12 m (C–LR12m) and 34 m (C–LR34m). Further details of the

218   experimental design are shown in appendix Fig. A1. This experiment is to

219   demonstrate the significant improvement that a fine vertical resolution can

220   achieve compared to the coarse resolution (e.g., tens of meters) that is often

221   adopted in slab ocean model.

222   (3) Shallow ocean bottom experiment: Three simulations with the ocean model

223   bottom at 10 m (C–HR1mB10m), 30 m (C–HR1mB30m), and 60 m (C–

224   HR1mB60m) (appendix Fig. A2). Note that all experiments retained the same

225   vertical resolution (e.g., 1 meter in the first top 10 meters of the ocean) but with

226   various ocean bottom (i.e., 10, 30, and 60 meters). The purpose is to demonstrate

227   how the total ocean heat content, which depends on the total depth of the ocean,

228   can affect the MJO.

229   (4) Regional coupling experiment: Four simulations with the coupling region in 0°N–

230   30°N (C–0_30N) and 0°S–30°S (C–0_30S) for latitudinal effect, and 30°E–

231   180°E (C–30_180E) and 30°E–75°W (C–30E_75W) for longitudinal effect. The

232   coupling domains are shown in Fig. 1. In this experiment we identified the key

233   ocean basins where coupling is essential.

234   (5) Diurnal cycle experiment: To explore the effect of diurnal coupling cycle a non-

235   diurnal simulation was conducted for a comparison with the C–30NS simulation.

236   The non-diurnal simulation (C–30NS–nD) considers the air–sea interaction only

237   once a day, namely, calculating SHF and LHF based on daily mean atmospheric

238   variables and SST. To prevent the inconsistent local time in different regions, the

239   coupling frequency at each grid point remained 48 times per day using the same

240   daily means of atmospheric variables and SST at that particular point. In

241   contrast, the control simulation calculates air–sea fluxes 48 times a day based on

242   instantons values. A comparison between the non-diurnal simulation and the

243   control simulation reveals the effect of diurnal cycle in air–sea coupling.

244

245   **3. Results and Discussion**

246   The realistic simulation of the MJO has always been a major bottleneck in the

247   development of climate models. In this section, we demonstrate the sensitivity of air–

248   sea coupling experiments using a 1-D high-resolution ocean model significantly

249   improves the MJO simulation by the CAM5.3. The period between November and

250   April when the MJO is the most prominent was the targeted season in this study.

251

252   **3.1 Improvement of MJO simulation through air–sea coupling**

253   This subsection compares the MJO simulation of the control coupled

254   experiment (C–30NS) with that of the uncoupled AGCM (A–CTL) forced by

255   climatological monthly SST of HadISST1 to demonstrate the effect of air–sea

256   coupling on the MJO simulation by coupling the SIT model to the CAM5.3 in the

257   tropical belt (30°N–30°S).

258

259   **3.1.1 Wavenumber–frequency spectra and eastward propagation characteristics**

260   A wavenumber–frequency spectrum (W–FS) analysis was conducted to quantify

261   propagation characteristics simulated in different experiments. The spectra

262   of unfiltered U850 in ERA-I reanalysis, C–30NS, and A–CTL are shown in Fig. 2a–c,

263   respectively. The C–30NS considering the coupling in 30ºN–30ºS realistically

264   simulates eastward-propagating signals at zonal wavenumber 1 and 30–80-day

265   periods (Fig. 2a–b), although with a slightly larger amplitude compared with ERA-I.

266   By contrast, the uncoupled A–CTL does not yield realistic simulation; instead, it

267   simulates both eastward (wavenumber 1)- and westward (wavenumber 2)-propagating

268   signals with an unrealistic spectral shift to time scales longer than 30–80-day.

269   The major features of the simulated MJO propagation were examined. Figure

270   2d–f show the time evolution of precipitation and U850 anomalies in Hovmöller

271   diagrams, which represent lagged correlation coefficients between the precipitation

272   averaged over 10°S–5°N, 75–100°E and the precipitation and U850 averaged over

273   10°N–10°S on intraseasonal timescales. Figure 2d indicates eastward propagation for

274   both precipitation and U850 from the eastern IO to the dateline, with precipitation

275   leading U850 by approximately a quarter of a cycle. The Hovmöller diagram derived

276   from the C–30NS (Fig. 2e) exhibits the key characteristics of eastward propagation

277   for both precipitation and U850 and the relative phases between the two, although the

278   simulated correlation is slightly weaker than that derived from GPCP and ERA-I. By

279   contrast, the uncoupled A–CTL simulates intraseasonal signals that propagate

280   westward over the IO and weak and much slower eastward propagation crossing the

281   MC and WP (Fig. 2f). The contrast between Fig. 2e and 2f demonstrate that coupling

282   a 1-D TKE ocean model alone could lead to a significant improvement in an AGCM

283   in simulating the major characteristics (e.g., amplitude, propagation direction and

284   speed, and phase relationship between precipitation and circulation) of the MJO.

285

286   **3.1.2 Coherence of the simulated MJO**

287   Cross-spectral analysis was conducted to examine the coherence and phase lag

288   between tropical circulation and convection, which were plotted over the tropical

289   wave spectra. Figure 2g–i show the symmetric part (e.g., Wheeler and Kiladis, 1999)

290   of OLR and U850 in ERA-I/NOAA data, C–30NS, and A–CTL, respectively. We

291   present only the spectra between 0 to 0.35 day^{-1} to highlight the MJO and equatorial

292   Kelvin waves. The most prominent characteristics seen in ERA-I/NOAA data are the

293   peak coherence at wavenumbers 1–3 and a phase lag of approximately 90° in the 30–

294   80-day band (Ren et al., 2019; Wheeler and Kiladis 1999). The coupled experiment

295   C–30NS simulates strong coherence in this low-frequency band (wavenumber 1) and

296   exhibits a realistic phase lag relationship between U850 and OLR perturbations.

297   However, the coherence at wavenumbers 2–3 for the 30–80-day period simulated by

298   C–30NS is weaker than that in ERA-I/NOAA data. This undersimulation was also

299   noted in CCSM4 (Subramanian et al., 2011), the uncoupled and coupled CAM4 and

300   CAM5 (Li et al., 2016), and NorESM1-M (Bentsen et al., 2013), which had a version

301   of the CAM as an AGCM. In summary, C–30NS considering the coupling between

302   30°N–30°S produces coherent and energetic patterns in the eastward-propagating

303   intraseasonal fluctuations of U850 and OLR in the tropical IO and WP that are

304   generally consistent with the MJO characteristics. By contrast, the MJO

305   characteristics in A–CTL are considerably weaker than those in C–30NS and that in

306   ERA-I/NOAA data.

307

3.1.3 Horizontal and vertical structures of the MJO across the MC

309   Figure 2j–o show the horizontal and vertical structures of the MJO when deep

310   convection is the strongest over the MC (i.e., phase 5). Figure 2j–l present the 20–

311   100-day filtered OLR (W m^{-2}, shaded) and 850-hPa wind (m s^{-1}, vector). C–30NS

312   realistically simulated the enhanced tropical convection over the eastern IO and the

313   Kelvin-wave-like easterly anomalies over the tropical WP despite undersimulating

314   the convection over the MC (Fig. 2j and 2k). By contrast, A–CTL failed to simulate

315   the enhanced convection over the eastern IO and MC; instead, it simulated

316   considerably weaker convection and easterly winds over the MC and WP,

317   respectively, than that in ERA-I/NOAA data (Fig. 2j and 2l).

318   Figure 2m–o show the vertical–longitudinal profiles of 20–100-day filtered

319   15°N–15°S averaged vertical velocity (OMEGA; Pa s^{-1}, shaded) and moist static

320   energy tendency (dMSE/dt) anomalies (W m^{-2}, contour) at phase 5. The spatial

321   distribution of negative OMEGA (ascending motion) anomalies generally agreed with

322   OLR anomalies in C–30NS simulation and NOAA data over the Indo-Pacific region

323   (Fig. 2m and 2n). The relatively spatial relationship between the ascending motion

324   and dMSE/dt seen in ERA-I is well simulated in the coupled experiment C–30NS. For

325   example, positive dMSE/dt anomalies on the eastern side of the anomalous ascent

326   demonstrate that the energy recharge process occurs in advance of the MJO

327   convection over the lower-tropospheric easterlies (Fig. 2m and 2n), whereas negative

328   dMSE/dt anomalies on the western side reveal that the discharge process occurs

329   during and after convection over the lower-tropospheric westerlies. By contrast, this

330   phase relationship, considered to be an essential feature leading to the eastward

331   propagation of an MJO (Hannah and Maloney 2014; Heath et al., 2021), is not

332   properly simulated in the uncoupled experiment A–CTL (Fig. 2o), in which the

333   simulated weak negative OMEGA is located between negative and positive dMSE/dt

334   anomalies over weak lower-tropospheric wind anomalies and associated with weak

335   convection over the MC (Fig. 2l).

336   The temporal evolution of NOAA OLR and ERA-I U850 (Fig. 3a) indicates

337   that convection originating in the western IO is enhanced during its eastward

338   propagation to the MC where it reaches the peak amplitude and then gradually

339   weakened when continuing moving eastward to the dateline. In the coupled

340   experiment C–30NS, this evolution of convectively coupled circulation is realistically

341   simulated, although it is weaker than the strength seen in NOAA OLR (Fig. 3b).

342   Moreover, the split of convection into two cells off the equator in phase 6 is

343   appropriately simulated in C–30NS (P6 in Fig. 3a and 3b). This split was caused by

344   the topographic and land–sea contrast effects of the MC (Tseng et al., 2017).

345   Associated with the split is the southward detouring of the anomalous convection

346   during the passage of the MJO through the MC (Kim et al. 2017, Tseng et al., 2017;

347   Wu and Hsu, 2009). After the passage of the MJO through the MC, the anomalous

348   convection stays south of the equator and continues moving eastward to the

349   dateline. In the uncoupled A–CTL, the systematic eastward propagation of

350   convectively coupled MJO circulation from the IO into the MC is not simulated.

351   Instead, the convection over the MC develops in situ at a later stage than that

352   observed (e.g., P6 in Fig. 3c) and dissipated rapidly. The A–CTL simulates a pair of

353   off-equator convection anomalies in the eastern IO during phase 2 (P2 in Fig. 3c) that

354   moves westward toward the central IO and were amplified at later stages (e.g., P4 in

355   Fig. 3c). This unrealistic evolution explains the westward propagation tendency

356   observed in the Hovmöller diagram (Fig. 2f).

357

358   **3.1.4 Characteristics of air–sea interaction**

359   Figure 4a–c show the longitude–phase diagram in which the 20–100-day filtered

360   precipitation (shaded) and SST (contour) anomalies were averaged over 10°S–10°N to

361   determine the relationship between precipitation and SST fluctuations and to establish

362   a link between air–sea coupling and convection. The propagation of the enhanced

363   convection with positive SST anomalies to the east could be clearly seen in

364   GPCP/OISST and the coupled experiment C–30NS (Fig. 4a and 4b). The highest SST

365   anomaly (SSTA) leads the maximum precipitation anomaly by approximately 2–3

366   phases, and the SSTA begins to decrease following the onset of enhanced

367   precipitation. The ERA-I and OISST data reveal the following relationship between

368   net surface flux and SST: the decreased (increased) LHF/SHF and increased

369   (decreased) downward radiation flux leading (lagging) the positive (negative) SSTA

15

370　east (west) of anomalous deep convection. This well-known lead–lag relationship

371　reflecting the active air–sea interaction in an MJO is realistically simulated in the

372　coupled experiment C–30NS (not shown).

373　　　　The contrast between C–30NS and A–CTL confirms the key role of the air–sea

374　interaction in contributing to the eastward propagation and demonstrates that the

375　eastward propagation simulation can be markedly improved by incorporating the air–

376　sea interaction process in the model, even when using a simple 1-D ocean model such

377　as SIT.

378

379　**3.1.5 Vertically tilting structure**

380　　　　The warm SST was the key forcing that contributed to the boundary layer

381　convergence before the onset of deep convection (Li et al., 2020; Tseng et al., 2014).

382　Hence, the warmer upper ocean enhances the low-level atmospheric convergence and

383　then leads to enhanced low-level moisture and preconditioned deep convection and

384　eastward propagation. This moistening process associated with warm ocean surface

385　temperature is well simulated in the coupled experiment C–30NS but is not shown

386　here. Instead, we present the coupling of moisture divergence (MD) and atmospheric

387　circulation.

388　　　　MD and zonal wind anomalies from the surface to the upper troposphere

389　averaged over the 10°S–10°N and 120–150°E region are shown in Fig. 4d–f to depict

390　the relationship between the vertically tilting structure of MD and zonal wind

391　anomalies. Note that the active convection occurred around phase 5. The coupled

392　experiment C–30NS (Fig. 4e) realistically simulates the deepening of coupled MD

393　and zonal wind anomalies with time (Fig. 4d). An evolution from the right to left

394　seen in each panel of Fig. 4d–f is equivalent to the eastward movement of vertically

395　tilting circulation from the eastern IO into the MC because of the eastward-

396   propagating nature of the MJO. Figure 4d and 4e show that in both ERA-I reanalysis

397   and the coupled experiment C–30NS, the near-surface convergence (negative MD)

398   occurring in the easterly anomalies lead the convection and continued deepening up

399   to 500 hPa from phase 2 to phase 6 when the easterly anomalies switch to westerly

400   anomalies. By contrast, this evolution of coupled MD–zonal wind anomalies are not

401   appropriately simulated in the uncoupled experiment (Fig. 4f). For example, a slow

402   deepening with time is observed in the MD anomaly but not in the zonal wind

403   anomaly that exhibits a vertically decayed structure, suggesting that MD and wind

404   anomalies are not well coupled, as noted in the ERA-I/NOAA data and the control

405   coupled experiment.

406   In the ERA-I reanalysis data, the negative near-surface MD anomalies appear

407   first under the easterly anomaly and continue deepening between the easterly and

408   westerly anomalies. This development in the phase relationship between MD and

409   zonal wind anomalies in both ERA-I reanalysis data and the coupled simulation is

410   consistent with the well-known structure embedded in the MJO, namely the near-

411   surface convergence in the easterly phase (i.e., a boundary-layer moistening process;

412   Kiranmayi and Maloney 2011; Li et al., 2020; Tseng et al., 2014), followed by the

413   deep convection when transitioning to the westerly phase. This close phase

414   relationship that is key to the eastward propagation is appropriately simulated in the

415   coupled experiment but not in the uncoupled experiment.

416

417   **3.1.6 Intraseasonal variance of precipitation**

418   Figure 4g–i present the spatial distribution of intraseasonal variance of

419   precipitation. In the GPCP data, the maximum variance is noted over the tropical

420   eastern IO, MC, and tropical WP. The maximum variance south of the island in the

421   MC and the equator in the tropical WP reflects the southward shift of the MJO deep

422   convection when passing through the MC, partly due to the blocking effect of

423   mountainous islands and the higher moisture content over high SST south of the

424   equator in the region during boreal winter (Kim et al., 2017; Ling et al., 2019; Sobel

425   et al., 2008; Tseng et al., 2017; Wu and Hsu, 2009). Although the control coupled

426   experiment fails to simulate the variance maximum in the tropical eastern IO, it

427   appropriately simulates the maximum variance over the tropical WP, reflecting its

428   ability to simulate the eastward propagation of the MJO through the MC. By contrast,

429   the uncoupled A–CTL experiment simulates considerably weaker intraseasonal

430   variance in both the tropical eastern IO and the tropical WP. Figure 4j–l are the 20–

431   100-day filtered SST (K, shaded) and 850-hPa wind (m s^{-1}, vector) during MJO

432   phase 7 when deep convection is the strongest over the dateline. The coupled

433   experiment C–30NS realistically simulates the negative SST anomaly over the MC

434   and WP when enhanced tropical convection passed through the MC to the dateline,

435   indicating the capability of the SIT model to reproduce the SST anomaly by

436   exchanging LHF/SHF between the atmosphere and ocean. In A-CTL, no SST

437   anomaly is evident because the model was forced by prescribed climatological SST.

438   The contrast seen in Fig. 4j–l demonstrates the essential role of atmosphere–ocean

439   coupling in shaping the MJO. A delayed air–sea interaction mechanism was noted,

440   where a preceding active-phase MJO may trigger an inactive-phase MJO through the

441   delayed effect of the induced SST anomaly. In addition, the westerly winds at 850

442   hPa moving southward between MC and WP are captured by the control experiment

443   C–30NS and are similar to the ERA-I reanalysis winds (Fig. 4j and 4k). By contrast,

444   A–CTL forced by climatological monthly SST (<0.05 K phase^{-1} anomaly) fails to

445   simulate the southward westerly wind of the region extending from the MC to the

446   dateline (Fig. 4l).

447

3.2 Effect of upper-ocean vertical resolution

448

449 In the control coupled experiment C–30NS, the vertical resolution in the upper

450 10.5 m was 1 m. Tseng et al. (2014) suggested that fine vertical resolution is crucial

451 for appropriately simulating the eastward propagation. To investigate the effect of

452 vertical resolution, two experiments with a thicker first layer were conducted by

453 moving the center of the layer to 11.5 m (C–LR12m) and 33.9 m (C–LR34m),

454 respectively, as opposed to the control experiment in which 10 layers were

455 implemented in the first 10.5 meters (see appendix Fig. A1 for vertical discretization).

456 The dramatic changes in vertical profile of ocean temperature between the fine and

457 coarse resolution simulation are demonstrated in Fig.5, which presents the 20–100-

458 day filtered oceanic temperature anomalies (K, shaded) between 0 and 60 m depth for

459 MJO phase 1, 3, 5, and 7. The amplitude of ocean temperature is the largest in C–

460 30NS and much weaker in C–LR12m and C–LR34m. In addition, there is a clear

461 vertical stratification of ocean temperature in C–30NS, whereas C–LR12m and C–

462 LR34m are well mixed because of not vertically gridded. This demonstrates the

463 necessity of fine vertical gridding for resolving the quick fluctuation of ocean

464 temperature when interacting with the atmosphere.

465 The W–FS spectral peaks of U850 in C–LR12m are concentrated in eastward-

466 propagating wavenumber 1 at three timescales (e.g., longer than 80 days, 30–80 days,

467 and approximately 30 days; Fig. 6a). In C–LR34m, both eastward and westward

468 signals are simulated with the dominant W–FS timescale longer than 80 days (Fig.

469 6b). The appearance of both eastward and westward signals at a lower frequency

470 implied a stronger stationary tendency or weaker eastward-propagating tendency. This

471 result is consistent with that reported by Tseng et al. (2014) that the scientific

472 reproducibility of coarser resolution causes a longer intraseasonal periodicity and

473 slower eastward propagation of the MJO.

474   The effect of vertical resolution on the MJO simulation can be seen in the

475   Hovmöller diagram. The eastward propagation simulated in C–LR12m (Fig. 6c)

476   markedly weakened after crossing the MC compare with that simulated in the control

477   experiment C–30NS (Fig. 2e). In C–LR34m, the quasi-stationary fluctuation and

478   westward propagation are simulated over the IO (Fig. 6d), appearing similar to those

479   in A–CTL (Fig. 2f). The lead–lag relationship between precipitation (zonal wind) and

480   SST is poorly simulated in C–LR12m (Fig. 6e) and even more poorly simulated in C–

481   LR34m (Fig. 6f). This result confirms the finding reported by Tseng et al. (2014) that

482   a higher vertical resolution in the upper few meters below the surface allows for a

483   faster air–sea interaction, thus resulting in a more realistic simulation of the MJO.

484

485   **3.3 Effect of the lowest boundary of the SIT model**

486   The ocean is a vital energy source for the MJO. Although vertical resolution is

487   crucial for the efficiency of air–sea interaction, the thickness of the upper ocean that

488   interacts with the atmosphere represents the ocean heat content to substantiate the

489   MJO. A key question is how the total ocean heat content, which depends on the total

490   depth of the ocean, can affect the MJO. Considering two models with the same

491   vertical resolution, the model with thinner ocean (e.g., 10 meter) would interact as

492   efficiently as another model with thicker ocean (e.g., 60m) but with much less heat to

493   release to or to absorb from the atmosphere. The former would have less impact on

494   the atmosphere than the latter. Using the same vertical resolution, three experiments

495   with various ocean depths ocean bottom at 10, 30, and 60 m were conducted (see

496   appendix Fig. A2 and Table 1).

497   The spectra and the Hovmöller diagrams shown in Fig. 7a–c and Fig. 7d–f,

498   respectively, demonstrate that the thicker ocean model simulates a stronger MJO with

499   a frequency closer to those in the coupled experiment C–30NS and ERA-I/NOAA

500   data, and more realistic eastward propagation. In addition, the lead–lag relationship

501   between precipitation (wind) and SST is more realistically simulated with increasing

502   thickness of the ocean model (Fig. 7g–i).

503   This result suggests that the thickness of the vertically-gridded ocean that interacts

504   with the atmosphere strongly affects the frequency of the simulated MJO. A thinner

505   (thicker) vertically-gridded ocean is more quickly (slowly) recharged and discharged

506   through SHF and LHF exchange between the atmosphere and ocean and therefore

507   likely fluctuates at a faster (slower) tempo. The simulated periodicity is therefore

508   affected by the thickness (or ocean heat content) of upper ocean that interacts

509   rigorously with the atmosphere. Although the result suggests 60 m is an appropriate

510   thickness to realistically simulate the periodicity of the MJO, we did not intend to

511   suggest the exact thickness required for a proper simulation because it might depend

512   on the model. The upper ocean should be adequately thick to contain a certain amount

513   of heat to generate appropriate periodicity. However, the reason for the intraseasonal

514   time scale (i.e., 20-100 days) should be determined in future studies. This finding

515   does not suggest a constant periodicity because periodicity might be affected by the

516   time-varying structure of the atmosphere and ocean in the real world.

517

518   **3.4 Effects of coupling domains**

519   The MJO is a planetary-scale phenomenon. Given its large-scale circulation, the

520   air–sea interaction affecting the MJO likely occurs in a much larger area than the

521   region near the major convection anomalies. In this section, we discuss the effect of

522   coupling domain on model ability to simulate the eastward propagation speed and

523   periodicity of the MJO. Four experiments considering the coupling in various

524   domains (C–0_30N, C–0_30S, C–30_180E, and C–30E_75W, Fig. 1) were conducted

525   for the purpose. The results are shown in Fig. 8. The C–0_30N that considered the

526   coupling in the tropics between the equator and 30°N simulates the least realistic MJO

527   propagation in terms of W–FS (Fig. 8a), zonal wind–precipitation coupling (Fig. 8e),

528   and SST–precipitation (Fig. 8i) among the four regional coupling experiments. By

529   contrast, coupling only the tropics between the equator and 30°S simulates a more

530   realistic MJO in all three aspects (i.e., spectrum in Fig. 8b, temporal evolution of

531   precipitation/wind, and precipitation/SST coupling in Fig. 8f and 8j). Figure. 9a

532   indicates that the negative OLR anomalies at phase 5 simulated in C–0_30N stays

533   mainly north of the equator and does not shift southward in the MC as revealed in

534   ERA-I reanalysis and NOAA OLR and in the control experiment C–30NS, and the

535   convection over the IO is unrealistically weak. By contrast, the southward detouring

536   in the MC is realistically simulated in C–0_30S that coupled only the tropical ocean

537   between the equator and 30°S. This result indicates that air–sea coupling occurring

538   south of the equator is the key to producing appropriate eastward propagation and

539   detouring of the MJO through the MC. Without this coupling, the C–0_30N

540   experiment fails to realistically simulate the eastward propagation of the MJO (Fig.

541   8e). This contrast can be attributed to the warmer ocean surface and higher moisture

542   content found south of the equator in boreal winter, which comprise a more favorable

543   environmental condition for air–sea coupling and convection–circulation coupling and

544   the occurrence of the MJO.

545   MJO simulations can be affected by air–sea coupling in the longitudinal domain.

546   Tseng et al. (2014) examined this effect by allowing coupling in different regions

547   (e.g., the IO, WP, and IO + WP) and found that the IO + WP coupling experiment

548   yielded the most satisfactory MJO simulation in terms of the zonal W–FS and

549   eastward propagation characteristics. In this study, we conducted sensitivity

550   experiments in which we allowed coupling in the tropics in two longitudinal domains,

551   namely 30°E–180°E (C–30_180E) and 30°E–75°W (C–30E_75W). The 30°E–180°E

552   region covered the IO and WP, and the 30°E–75°W region covered the IO and the

553   entire tropical Pacific. As shown in Fig. 8, the C–30E_75W experiment simulates

554   more realistic MJO than the C–30_180E experiment, with stronger eastward

555   propagation and larger amplitudes in the spectrum (Fig. 8c and 8d) and Hovmöller

556   diagrams of precipitation/wind (Fig. 8g and 8h) and precipitation/SST (Fig. 8k and

557   8l). The simulated MJO in C–30E_75W propagated farther east than that in C–

558   30_180E, particularly evident in Fig. 8k and 8l. The spatial distributions of circulation

559   and OLR shown in Fig. 9c and 9d indicate the presence of a stronger convective-

560   coupled circulation system over the MC and WP in C–30E_75W. These results

561   suggest that coupling over the entire tropical IO and Pacific could enhance the

562   strength and eastward propagation of the MJO and encourage farther propagation to

563   the central Pacific.

564

565   **3.5 Diurnal versus no diurnal cycle in air–sea coupling**

566   Previous studies showed that the diurnal cycle in the MC can weaken the MJO

567   and its eastward propagation (Hagos et al., 2016; Oh et al., 2013). We conducted an

568   experiment to determine whether computing surface heat fluxes using daily mean

569   values, instead of instantaneous values, of atmospheric variables and SST with the

570   same coupling frequency would affect the MJO simulation. The coupling in the model

571   was conducted through the SHF and LHF exchange between the atmosphere and

572   ocean, that were calculated based on simulated winds, moisture, and temperature. As

573   mentioned in Section 2.3, air–sea fluxes were calculated twice for every time step

574   (coupling 48 times per day) in the control coupled experiment (C–30NS) based on the

575   instantaneous values of atmospheric and oceanic variables. In the experiment in which

576   the diurnal cycle was removed (C–30NS–nD), air–sea fluxes were calculated as in C–

577   30NS but were based on daily means of both atmospheric variables and SST. Doing

578　this removed certain diurnal effects of air-sea coupling. The results shown in Fig. 10

579　reveal the enhancement of the eastward-propagating signals in the MJO (e.g., a larger

580　amplitude in spectrum; Fig. 10a) and further eastward propagation (Fig. 10b) as well

581　stronger coupling between precipitation and SST (Fig. 10c) in C–30NS–nD. The

582　overall results are consistent with previous finding that the diurnal cycle tends to

583　reduce the amplitude of the MJO, indicating that the weakening effect occurs through

584　air–sea coupling in addition to those processes in the atmosphere. Previous studies

585　have hypothesized that rapid interaction processes in the diurnal time scale tend to

586　extract energy from the MJO, thus reducing the strength and propagation tendency of

587　the MJO. However, a comparison between the spectra of C–30NS and C–30NS–nD

588　indicates that the experiment in which the diurnal cycle is removed appeared to

589　oversimulate the MJO with unrealistic strength, suggesting that the effect of the

590　diurnal cycle should be considered in the model to simulate a more realistic MJO.

591　However, whether this is a common result in different models remain to be examined.

592

593　**4. Discussion and conclusions**

594　　　Air–sea coupling is a key mechanism for the successful simulation of the MJO

595　(Chang et al., 2019; DeMott et al., 2015; Jiang et al., 2015, 2020; Kim et al., 2010; Li

596　et al., 2016; Li et al., 2020; Newman et al., 2009; Tseng et al., 2014). This study,

597　following the study of Tseng et al. (2014), demonstrated that coupling a high-

598　resolution 1-D TKE ocean model (namely the SIT model) to the CAM5, namely the

599　CAM5–SIT, significantly improved the MJO simulation over the standalone CAM5.

600　By coupling SIT model to an AGCM different from Tseng et al. (2014), this study

601　confirms the scientific reproducibility for the improvement of MJO simulation in

602　modeling science. The CAM5–SIT realistically simulates the MJO characteristics in

603　many aspects (e.g., intraseasonal periodicity, eastward propagation, coherence in the

604   low-frequency band, detouring propagation across the MC, tilting vertical structure,

605   and intraseasonal variance in the WP).

606   Systematic sensitivity experiments were conducted to investigate the effects of

607   the vertical resolution and the thickness of the 1-D ocean model, coupling domains,

608   and the absence of the diurnal cycle. The results of all the sensitivity experiments are

609   summarized in Fig. 11a and 11b, which show four common metrics for MJO

610   evaluation. The four metrics are the propagation speed of the MJO (estimated from

611   the U850 Hovmöller diagram as Fig. 2d–f) versus the power ratio of eastward- and

612   westward-propagating 30–80-day signals (E/W ratio, derived from the zonal W–FS)

613   in Fig. 11a and the eastward propagation speed of the 30–80-day filtered precipitation

614   anomaly (estimated from the precipitation Hovmöller diagram) versus the variance

615   explained by RMM1 and RMM2 (i.e., the sum of the variance explained by the first

616   two empirical orthogonal functions (EOF1 and EOF2) based on Wheeler and Hendon,

617   2004) in Fig. 11b. Based on the maximum precipitation anomaly and zero values of

618   U850 (indicating deep convection region), propagation speeds of precipitation and

619   U850 were calculated from Hovmöller diagrams between 60°E and 150°W. Overall,

620   the control experiment C–30NS simulates the most realistic MJO among all

621   sensitivity experiments.

622   As for vertical resolution, we determined that the MJO simulation efficiency

623   decreased when the vertical resolution of the SIT model is decreased from 1 m to 11.5

624   or 33.9 m, as simulated in the C–LR12m and C–LR34m experiments, respectively.

625   This finding, consistent with that reported by Tseng et al. (2014), suggests that a finer

626   vertical resolution more effectively resolves temperature variations in the ocean warm

627   layer and enhances atmospheric–ocean coupling, thus enabling the upper ocean to

628   more efficiently respond to atmospheric forcing by providing sensible and latent heat

629   fluxes; this results in superior synchronization between the lower atmosphere and the

25

630   upper ocean.

631   We observed that the shallower ocean model bottom could speed up the eastward

632   propagation of the MJO by producing more perturbations of shorter periodicity (Fig.

633   7) and results in a weaker MJO. The shallower ocean layer with vertical grids likely

634   responds more quickly to atmospheric forcing but provides less sensible and latent

635   heat fluxes to the atmosphere. Thus, the MJO propagates too fast with a weaker

636   amplitude.

637   In the coupling domain sensitivity experiments, we investigated the essential

638   coupling domain required to simulate the realistic MJO and the effect of the domain

639   on the MJO simulation. Coupling only the northern tropics fails to simulate the

640   eastward propagation, whereas coupling only the southern tropics yields a more

641   realistic MJO simulation, although this simulation is inferior to coupling the entire

642   tropics. This contrast reveals the importance of the southern tropical ocean, especially

643   in the MC where high SST and moisture content are noted. Coupling in the southern

644   tropics is therefore essential for providing the energy required to maintain the MJO

645   and its eastward propagation. By contrast, the northern tropics are relatively dry and

646   cool. Coupling in this region is therefore less effective in improving MJO simulation.

647   In the longitudinal domain sensitivity experiments, we found that the MJO

648   amplitude and the eastward extend of its eastward propagation are enhanced by

649   extending the eastern boundary of the coupling domain from the tropical eastern IO to

650   the tropical WP and further to the tropical eastern Pacific (Fig. 1). Further extension

651   of the domain to cover the tropical Atlantic does not exhibit further enhancement (not

652   shown). This result indicates that coupling in the tropical central and eastern Pacific,

653   although not the major MJO signal regions (i.e., from the tropical IO to the tropical

654   WP), still played a marked role in sustaining the MJO. We propose the following to

655   explain this effect. Because of the planetary scale of the MJO, the near-surface

26

656 easterly circulation to the east of the convection core often extended to the tropical

657 central and eastern Pacific where the climatological easterly prevailed. The coupling

658 beyond the WP increased low-level moisture transport and convergence to the east of

659 the convection and establish an environment suitable for the further eastward

660 propagation of the MJO. This effect was likely terminated by the landmass of Central

661 America when the tropical Atlantic was further included. Thus, a further eastward

662 extension of the coupling domain exerted little effect on further enhancing the MJO. A

663 diagnostic study on the effect of the longitudinal coupling domain is being conducted,

664 and the results will be reported in a following paper.

665 　　The diurnal versus nondiurnal cycle experiment indicates that nondiurnal

666 coupling tended to enhance eastward-propagating signals but slow down the eastward

667 propagation (Fig. 11a–b). This result is consistent with the finding of previous studies

668 that the diurnal cycle in the atmosphere extracts energy from the MJO, thus

669 weakening it.

670 　　In this study, we demonstrated how air–sea coupling can improve the MJO

671 simulation in a GCM. The findings are as follows.

672 (1) Better resolving the fine structure of the upper-ocean temperature and therefore

673 　　the air–sea interaction leads to more realistic intraseasonal variability in both

674 　　tropical SST and atmospheric circulation.

675 (2) An adequate thickness of vertically-gridded upper ocean is required to simulate a

676 　　delayed response of the upper ocean to atmospheric forcing and lower-frequency

677 　　fluctuation.

678 (3) Coupling the tropical eastern Pacific, in addition to the tropical IO and the tropical

679 　　WP, can enhance the MJO and facilitate the further eastward propagation of the

680 　　MJO to the dateline.

681 (4) Coupling the southern tropical ocean, instead of the norther tropical ocean, is

682   essential for simulating a realistic MJO.

683   (5) Stronger MJO variability can be obtained without considering the diurnal cycle in

684   coupling.

685   Our study confirmed the effectiveness of air–sea coupling for improving MJO

686   simulation in a climate model and demonstrated how and where to couple. The

687   findings enhance our understanding of the physical processes that shape the

688   characteristics of the MJO.

689

695

696   *Author contributions.* HHH is the initiator and the primary investigator of the

697   Taiwan Earth System Model project. YYL is the CAM5–SIT model developer and

698   writes the majority part of the paper. WLT and LCJ assist in MJO analysis.

699

700   *Competing interests*. The authors declare that they have no conflict of interest.

701

713   **Reference**

714   Adler, R. F., Huffman, G. J., Chang, A., Ferraro, R., Xie, P.
715   P., Janowiak, J., Rudolf, B., Schneider, U., Curtis, S., Bolvin,
716   D., Gruber, A., Susskind, J., Arkin, P., and Nelkini, E.: The
717   Version 2.1 Global Precipitation Climatology Project (GPCP)
718   Monthly Precipitation Analysis (1979 -Present), J. Hydrometeor.,
719   4(6), 1147-1167, https://doi.org/10.1175/1525-
720   7541(2003)004<1147:TVGPCP>2.0.CO;2, 2003.

721   Ahn, M.-S., Kim, D., Kang, D., Lee, J., Sperber, K. R., and Glecker, P.
722   J., et al.: MJO propagation across the Maritime Continent: Are
723   CMIP6 models better than CMIP5 models? Geophys. Res. Lett., 47,
724   e2020GL087250, https://doi.org/10.1029/2020GL087250, 2020.

725   Ahn, M.-S., Kim, D., Sperber, K. R., Kang, I.-S., Maloney, E., Waliser,
726   D., and Hendon, H.: MJO simulation in CMIP5 climate models:
727   MJO skill metrics and process-oriented diagnosis, Clim.
728   Dyn., 49, 4023–4045, https://doi.org/10.1007/s00382-017-3558-4,
729   2017.

730   Alappattu, D. P., Wang, Q., Kalogiros, J., Guy, N., and Jorgensen, D.
731   P.: Variability of upper ocean thermohaline structure during a MJO
732   event from DYNAMO aircraft observations, J. Geophys. Res. -
733   Oceans, 122, 1122–1140, https://doi.org/10.1002/2016JC012137,
734   2017.

735   Amante, C., and Eakins, B. W.: ETOPO1 1 arc-minute globe relief
736   model: Procedures, data sources and analysis, NOAA Tech. Memo.
737   NESDIS NGDC-24, 19 pp., NOAA, Silver Spring, Md., 2009.

738   Behringer, D. W., and Xue, Y.: Evaluation of the global ocean data
739   assimilation system at NCEP: The Pacific Ocean. Eighth
740   Symposium on Integrated Observing and Assimilation Systems for
741   Atmosphere, Oceans, and Land Surface, AMS 84th Annual
742   Meeting, Washington State Convention and Trade Center, Seattle,
743   Washington, 11-15. Derber, J.C., and A. Rosati, 1989: A global
744   oceanic data assimilation system, J. Phys. Oceanogr., 19, 1333–
745   1347, https://ams.confex.com/ams/pdfpapers/70720.pdf, 2004.

746   Bentsen, M., Bethke, I., Debernard, J. B., Iversen, T., Kirkevåg, A.,
747   Seland, Ø., Drange, H., Roelandt, C., Seierstad, I. A., Hoose, C.,
748   and Kristjánsson, J. E.: The Norwegian Earth System Model,
749   NorESM1-M – Part 1: Description and basic evaluation of the

physical climate, Geosci. Model Dev., 6, 687–720,
https://doi.org/10.5194/gmd-6-687-2013, 2013.

Bernie, D., Guilyardi, E., Madec, G., Slingo, J., Woolnough, S., and
Cole, J.: Impact of resolving the diurnal cycle in an ocean–
atmosphere GCM. Part 2: a diurnally coupled CGCM, Clim.
Dynam., 31, 909–925, https://doi.org/10.1007/s00382-008-0429-z,
2008.

Boyle, J. S., Klein, S. A., Lucas, D. D., Ma, H.-Y., Tannahill, J., and
Xie, S.: The parametric sensitivity of CAM5's MJO, J. Geophys.
Res.-Atmos., 120, 1424–1444,
https://doi.org/10.1002/2014JD022507, 2015.

Bui, H. X., and Maloney, E. D.: Changes in Madden-Julian Oscillation
precipitation and wind variance under global warming, Geophys.
Res. Lett., 45, 7148–7155, https://doi.org/10.1029/2018GL078504,
2018.

Chang, M.-Y., Li, T., Lin, P.-L., and Chang, T.-H.: Forecasts of MJO
Events during DYNAMO with a Coupled Atmosphere-Ocean
Model: Sensitivity to Cumulus Parameterization Scheme, J.
Meteorol. Res., 33, 1016–1030, https://doi.org/10.1007/s13351-
019-9062-5, 2019.

CLIVAR MADDEN–JULIAN OSCILLATION WORKING GROUP:
MJO simulation diagnostics, J. Climate, 22, 3006–3030,
https://doi.org/10.1175/2008JCLI2731.1, 2009.

Crueger, T., Stevens, B., and Brokopf, R.: The Madden–Julian
Oscillation in ECHAM6 and the introduction of an objective MJO
metric, J. Climate, 26, 3241–3257, https://doi.org/10.1175/JCLI-D-
12-00413.1, 2013.

Danabasoglu, G., Lamarque, J.-F., Bacmeister, J., Bailey, D. A.,
DuVivier, A. K., and Edwards, J., et al.: The Community Earth
System Model Version 2 (CESM2), J. Adv. Model. Earth Syst., 12,
e2019MS001916, https://doi.org/10.1029/2019MS001916, 2020.

Dee, D. P., Uppala, S. M., Simmons, A. J., Berrisford, P., Poli, P.,
Kobayashi, S., Andrae, U., Balmaseda, M. A., Balsamo, G., Bauer,
P., Bechtold, P., Beljaars, A. C. M., van de Berg, L., Bidlot, J.,
Bormann, N., Delsol, C., Dragani, R., Fuentes, M., Geer, A. J.,
Haimberger, L., Healy, S. B., Hersbach, H., Hólm, E. V., Isaksen,
L., Kållberg, P., Köhler, M., Matricardi, M., McNally, A. P.,
Monge-Sanz, B. M., Morcrette, J.-J., Park, B.-K., Peubey, C., de
Rosnay, P., Tavolato, C., Thépaut, J.-N., and Vitart, F.: The ERA-
Interim reanalysis: configuration and performance of the data
assimilation system, Q. J. R. Meteorol. Soc., 137: 553–597,
https://doi.org/10.1002/qj.828, 2011.

de Szoeke, S. P., Skyllingstad, E. D., Zuidema, P., and Chandra, A.
S.: Cold pools and their influence on the tropical marine boundary

794   layer, J. Atmos. Sci., 74, 1149–1168. https://doi.org/10.1175/JAS-
795   D-16-0264.1, 2017.

796   Delworth, T. L., et al.: GFDL's CM2 global coupled climate models.
797   Part 1: Formulation and simulation characteristics, J. Climate, 19,
798   643–674, https://doi.org/10.1175/JCLI3629.1, 2006.

799   DeMott, C. A., Klingaman, N. P., and Woolnough, S. J.: Atmosphere-
800   ocean coupled processes in the Madden-Julian oscillation, Rev.
801   Geophys., 53, 1099–1154, https://doi.org/10.1002/2014RG000478,
802   2015.

803   DeMott, C. A., Klingaman, N. P., Tseng, W.-L., Burt, M. A., Gao, Y.,
804   and Randall, D. A.: The convection connection: How ocean
805   feedbacks affect tropical mean moisture and MJO propagation, J.
806   Geophys. Res.-Atmos., 124, 11,910–11,931,
807   https://doi.org/10.1029/2019JD031015, 2019.

814   Haertel, P.: Prospects for Erratic and Intensifying Madden-Julian
815   Oscillations, Climate, 8, 24, https://doi.org/10.3390/cli8020024,
816   2020.

817   Hannah, W. M., and Maloney, E. D.: The moist static energy budget in
818   NCAR CAM5 hindcasts during DYNAMO, J. Adv. Model. Earth
819   Syst., 6, 420–440, https://doi.org/10.1002/2013MS000272, 2014.

820   Hagos, S. M., Zhang, C., Feng, Z., Burleyson, C. D., Mott, C. De,
821   Kerns, B., Benedict, J. J., and Martini, M. N.: The impact of the
822   diurnal cycle on the propagation of Madden-Julian Oscillation
823   convection across the Maritime Continent, J. Adv. Model. Earth
824   Syst., 8, 1552–1564, https://doi.org/10.1002/2016MS000725, 2016.

825   He, S., Yang, S., and Li, Z.: Influence of Latent Heating over the Asian
826   and Western Pacific Monsoon Region on Sahel Summer
827   Rainfall, Sci. Rep. 7, 7680, https://doi.org/10.1038/s41598-017-
828   07971-6, 2017.

829   Heath, A., Gonzalez, A. O., Gehne, M., and Jaramillo, A.: Interactions
830   of large-scale dynamics and Madden-Julian Oscillation propagation
831   in multi-model simulations, J. Geophys. Res.-Atmos., 126,
832   e2020JD033988. https://doi.org/10.1029/2020JD033988, 2021.

833   Hong, X., Reynolds, C. A., Doyle, J. D., May, P., and O'Neill, L.:
834   Assessment of upper-ocean variability and the Madden-Julian
835   Oscillation in extended-range air–ocean coupled mesoscale
836   simulations, Dyn. Atmos. Oceans, 78, 89–105.
837   https://doi.org/10.1016/j.dynatmoce.2017.03.002, 2017.

838   Hung, M.-P., Lin, J.-L., Wang, W., Kim, D., Shinoda, T., and Weaver,
839   S. J.: MJO and convectively coupled equatorial waves simulated by
840   CMIP5 climate models, J. Climate, 26, 6185–6214,
841   https://doi.org/10.1175/JCLI-D-12-00541.1, 2013.

842   Hurrell, J. W., Holland, M. M., Gent, P. R., Ghan, S., Kay, J. E.,

Kushner, P. J., Lamarque, J.-F., Large, W. G., Lawrence, D., Lindsay, K., Lipscomb, W. H., Long, M. C., Mahowald, N., Marsh, D. R., Neale, R. B., Rasch, P., Vavrus, S., Vertenstein, M., Bader, D., Collins, W. D., Hack, J. J., Kiehl, J., and Marshall, S.: The community Earth system model: A framework for collaborative research, B. Am. Meteorol. Soc., 94, 1319–1360, https://doi.org/10.1175/BAMS-D-12-00121, 2013.

Jiang, X., et al.: Vertical structure and physical processes of the MaddenJulian oscillation: Exploring key model physics in climate simulations, J. Geophys. Res.-Atmos., 120, 4718–4748, https://doi.org/10.1002/2014JD022375, 2015.

Jiang, X., Adames, Á. F., Kim, D., Maloney, E. D., Lin, H., and Kim, H., et al.: Fifty years of research on the Madden-Julian Oscillation: Recent progress, challenges, and perspectives, J. Geophys. Res.-Atmos., 125, e2019JD030911, https://doi.org/10.1029/2019JD030911, 2020.

Johnson, R. H., and Ciesielski, P. E.: Multiscale variability of the atmospheric boundary layer during DYNAMO, J. Atmos. Sci., 74, 4003–4021, https://doi.org/10.1175/JAS-D-17-0182.1, 2017.

Kaylor, R. E.: Filtering and decimation of digital time series, Tech. Rep. Note BN 850, Institute for Physical Science and Technology, University of Maryland at College Park, 14 pp., 1977.

Kim, D., Sobel, A. H., Maloney, E. D., Frierson, D. M., and Kang, I.-S.: A systematic relationship between intraseasonal variability and mean state bias in AGCM simulations, J. Climate, 24, 5506–5520. https://doi.org/10.1175/2011JCLI4177.1, 2011.

Kim, D., Kim H., and Lee, M.-I.: Why does the MJO detour the Maritime Continent during austral summer? Geophys. Res. Lett., 44, 2579–2587, https://doi.org/10.1002/2017GL072643, 2017.

Kim, H.-M., Hoyos, C. D., and Webster, P. J. et al.: Ocean–atmosphere coupling and the boreal winter MJO, Clim Dynam., 35, 771–784, https://doi.org/10.1007/s00382-009-0612-x, 2010.

Kiranmayi, L., and Maloney, E. D.: Intraseasonal moist static energy budget in reanalysis data, J. Geophys. Res., 116, D21117, https://doi.org/10.1029/2011JD016031, 2011.

Lan, Y.-Y., Tsuang, B.-J., Tu, C.-Y., Wu, T.-Y., Chen, Y.-L., and Hsieh, C.-I.: Observation and Simulation of Meteorology and Surface Energy Components over the South China Sea in Summers of 2004 and 2006, Terr. Atmos. Ocean. Sci., 21, 325–342, https://doi.org/ 10.3319/TAO.2009.04.07.01(A), 2010.

Lee, H.-T., and NOAA CDR Program: NOAA Climate Data Record (CDR) of Daily Outgoing Longwave Radiation (OLR), Version 1.2, NOAA National Climatic Data

887   Center, https://doi.org/10.7289/V5SJ1HH2, 2011.

888 Li, T., Ling, J., and Hsu, P.-C.: Madden–Julian Oscillation: Its
889   discovery, dynamics, and impact on East Asia, J. Meteor. Res., 34,
890   20–42, https://doi.org/10.1007/s13351-020-9153-3, 2020.

891 Li, T., Tam, F., Fu, X., Zhou, T., and Zhu, W.: Causes of the
892   intraseasonal SST variability in the tropical Indian Ocean, Atmos.
893   Oceanic Sci. Lett., 1, 18–23,
894   https://doi.org/10.1080/16742834.2008.11446758, 2008.

895 Li, X., Tang, Y., Zhou, L., Chen, D., and Yao, Z.: Assessment of Madden–Julian
896   oscillation simulations with various configurations of CESM, Clim. Dynam.,
897   47, 2667–2690, https://doi.org/10.1007/s00382-016-2991-0, 2016.

898 Ling, J., Zhao, Y., and Chen, G.: Barrier effect on MJO propagation by
899   the Maritime Continent in the MJO Task Force/GEWEX
900   atmospheric system study models, J. Climate, 32, 5529–
901   5547, https://doi.org/10.1175/JCLI-D-18-0870.1, 2019.

902 Madden, R. A., and Julian, P. R.: Description of global-scale
903   circulation cells in the tropics with a 40-50 day period, J. Atmos.
904   Sci., 29, 1109-1123, https://doi.org/10.1175/1520-
905   0469(1972)029<1109:DOGSCC>2.0.CO;2, 1972.

906 Madden, R. A., and Julian, P. R.: Observations of the 40-50 day
907   tropical oscillation - A review, Mon. Weather Rev., 122, 814– 837,
908   https://doi.org/10.1175/1520-
909   0493(1994)122<0814:OOTDTO>2.0.CO;2, 1994.

910 Neale, R. B., et al.,: Description of the NCAR Community Atmosphere
911   Model (CAM 5.0), NCAR Tech. Note NCAR/TN-486+STR, 289
912   pp., Natl. Cent. for Atmos. Res, Boulder, Colo., 2012.

913 Newman, M., Sardeshmukh, P. D., and Penland, C.: How important is
914   air–sea coupling in ENSO and MJO evolution? J.
915   Clim., 22, 2958– 2977, https://doi.org/10.1175/2008JCLI2659.1,
916   2009.

917 Oh, J., Kim, B., and Kim, K. et al.: The impact of the diurnal cycle on
918   the MJO over the Maritime Continent: a modeling study
919   assimilating TRMM rain rate into global analysis, Clim.
920   Dynam., 40, 893–911, https://doi.org/10.1007/s00382-012-1419-8,
921   2013.

922 Pei, S., Shinoda, T., Soloviev, A., and Lien, R.-C.: Upper ocean
923   response to the atmospheric cold pools associated with the
924   Madden-Julian Oscillation, Geophys. Res. Lett., 45, 5020–5029,
925   https://doi.org/10.1029/2018GL077825, 2018.

926 Pujiana, K., Moum, J. N., and Smyth, W. D.: The role of subsurface
927   turbulence in redistributing upper-ocean heat, freshwater, and
928   momentum in response to the MJO in the equatorial Indian
929   Ocean, J. Phys. Oceanogr., 48, 197–

220, https://doi.org/10.1175/JPO-D-17-0146.1, 2018.

Rayner, N. A., Parker, D. E., Horton, E. B., Folland, C. K., Alexander, L. V., Rowell, D. P., Kent, E. C., and Kaplan, A.: Global analyses of sea surface temperature, sea ice, and night marine air temperature since the late nineteenth century, J. Geophys. Res., 108(D14), 4407, https://doi.org/10.1029/2002JD002670, 2003.

Ren, P. F., Gao, L., and Ren, H.-L. et al.: Representation of the Madden–Julian Oscillation in CAMSCSM, J. Meteor. Res., 33, 627–650, https://doi.org/10.1007/s13351-019-8118-x, 2019.

Reynolds, R. W., and Smith, T. M.: A high-resolution global sea surface temperature climatology, J. Clim., 8(6),1571–1583, https://doi.org/10.1175/1520-0442(1995)008<1571:AHRGSS>2.0.CO;2, 1995.

Schreck, C. J., Lee, H.-T., and Knapp, K. R.: HIRS outgoing longwave radiation—Daily climate data record: Application toward identifying tropical subseasonal variability, Remote Sens., 10, 1325. https://doi.org/10.3390/rs10091325, 2018.

Sobel, A. H., Maloney, E. D., Bellon, G., and Dargan, M. F.: The role of surface heat fluxes in tropical intraseasonal oscillations, Nat. Geosci., 1, 653–657, https://doi.org/10.1038/ngeo312, 2008.

Subramanian, A. C., Jochum, M., Miller, A. J., Murtugudde, R., Neale, R. B., and Waliser, D. E.: The Madden–Julian oscillation in CCSM4, J. Climate, 24, 6261–6282, https://doi.org/10.1175/JCLI-D-11-00031.1, 2011.

Tseng, W.-L., Tsuang, B.-J., Keenlyside, N. S., Hsu, H.-H. and Tu, C.-Y.: Resolving the upper-ocean warm layer improves the simulation of the Madden-Julian oscillation, Clim. Dynam., 44, 1487–1503, https://doi.org/10.1007/s00382-014-2315-1, 2014.

Tseng, W.-L., Hsu, H.-H., Keenlyside, N., Chang, C.-W. J., Tsuang, B.-J., Tu, C.-Y., and Jiang, L.-C.: Effects of Orography and Land–Sea Contrast on the Madden–Julian Oscillation in the Maritime Continent: A Numerical Study Using ECHAM-SIT, J. Climate, 30, 9725–9741, https://doi.org/10.1175/JCLI-D-17-0051.1, 2017.

Tu, C.-Y., and Tsuang, B.-J.: Cool-skin simulation by a one-column ocean model, Geophys. Res. Lett., 32, L22602, https://doi.org/10.1029/2005GL024252, 2005.

Wang, W., Saha, S., Pan, H.-L., Nadiga, S., and White, G.: Simulation of ENSO in the new NCEP Coupled Forecast System Model (CFS03), Mon. Wea. Rev., 133, 1574–1593, https://doi.org/10.1175/MWR2936.1, 2005.

Wang, W., Hung, M.-P., Weaver, S. J., Kumar, A., and Fu, X.: MJO prediction in the NCEP Climate Forecast System version 2, Clim. Dyn., 42, 2509–2520, https://doi.org/10.1007/s00382-013-1806-9,

973   2014.

974   Wheeler, M. C., and Hendon, H. H.: An all-season real-time
975   multivariate MJO index: development of an index for monitoring
976   and prediction, Mon. Weather Rev., 132, 1917–1932,
977   https://doi.org/10.1175/1520-
978   0493(2004)132<1917:AARMMI>2.0.CO;2, 2004.

979   Wheeler, M., and Kiladis, G. N.: Convectively coupled equatorial
980   waves: Analysis of clouds and temperature in the wavenumber-
981   frequency domain, J. Atmos. Sci., 56, 374– 399,
982   https://doi.org/10.1175/1520-
983   0469(1999)056<0374:CCEWAO>2.0.CO;2, 1999.

984   Woolnough, S. J., Vitard, F., and Balmaseda, M. A.: The role of the
985   ocean in the Madden–Julian oscillation: Implications for MJO
986   prediction, Quart. J. Roy. Meteor. Soc., 133, 117–128,
987   https://doi.org/10.1002/qj.4, 2007.

988   Wu, C.-H., and Hsu, H.-H.: Potential Influence of Topography on the
989   MJO in the Maritime Continent, J. Climate, 22, 5433–5448,
990   https://doi.org/10.1175/2009JCLI2825.1, 2009.

991   Yoneyama, K., Zhang, C., and Long, C.: Tracking pulses of the
992   Madden–Julian oscillation, Bull. Amer. Meteor. Soc., 94, 1871–
993   1891, https://doi.org/10.1175/BAMS-D-12-00157.1, 2013.

994   Zhang, C.: Madden-Julian oscillation, Rev. Geophys., 43, RG2003,
995   https://doi.org/10.1029/2004RG000158, 2005.

996   Zhang, C., and Yoneyama, K.: CINDY/DYNAMO field campaign:
997   Advancing our understanding of MJO initiation, In World
998   Scientific Series on Asia-Pacific Weather and Climate (pp. 339-
999   348). (World Scientific Series on Asia-Pacific Weather and
1000   Climate; Vol. Volume 9), World Scientific Publishing Co. Pte Ltd.
1001   https://doi.org/10.1142/9789813200913_0027, 2017.

1002   Table 1. List of experiments

Section	Category	Experiments	Description
3.1	Coupled or uncoupled	A–CTL	Standalone CAM5.3 forced by forced by the monthly mean Hadley Centre SST dataset version 1 climatology
		C–30NS (the control coupled experiment)	CAM5.3 coupled with SIT over the tropical domain (30°N–30°S), with 41 layers of finest vertical resolution (up to the seabed) and diurnal cycle; the frequency of CAM5 being exchanged with CPL is 48 times per day
3.2	Upper-ocean vertical resolution	C–LR12m	The first ocean vertical level starts at 11.5 m with 31 layers (beside SST and cool skin layer are 11.5 m, 29.5 m and 43.6 m up to the seabed)
		C–LR34m	The first ocean vertical level starts at 33.9 m with 28 layers (beside SST and cool skin layer are 33.9 m, 76.9 m and 96.8 m up to the seabed)
3.3	Lowest boundary of SIT	C–HR1mB10m	The lowest boundary of SIT has a depth of 10 m (model depth between 0 m and 10 m)
		C–HR1mB30m	The lowest boundary of SIT has a depth of 30 m (model depth between 0 m and 30 m)
		C–HR1mB60m	The lowest boundary of SIT has a depth of 60 m (model depth between 0 m and 60 m)
3.4	Regional coupling domain in latitude	C–0_30N	Coupled in the tropical northern hemisphere (0°N–30°N, 0°E–360°E)
		C–0_30S	Coupled in the tropical southern hemisphere (0°S–30°S, 0°E–360°E)
	Regional coupling domain in longitude	C–30_180E	Coupled in the Indo-Pacific (30°N–30°S, 30°E–180°E)
		C–30E_75W	Coupled over the Indian Ocean and Pacific Ocean (30°N–30°S, 30°E–75°W)
3.5	Absence of the diurnal cycle	C–30NS–nD	Absence of the diurnal cycle in C–30NS; the CAM5.3 daily atmospheric mean of surface wind, temperature, total precipitation, net surface heat flux, u-stress and v-stress over water trigger the SIT and daily mean SST feedback to atmosphere; the frequency of CAM5 is exchanged with CPL 48 times per day

1003   Experiment abbreviations: "A" means standalone AGCM simulation. "C" means the

1004   CAM5.3 coupled to the SIT model.

1005 **Figure List**

1006 **Figure 1.** Schematics of coupled and uncoupled domains in the regional coupling

1007 experiment: (a) C–30NS, (b) C–0_30N, (c) C–0_30S, (d) C–30_180E, and (e) C–

1008 30E_75W. The background is the climatological mean SST in December–February (DJF).

1009

1010 **Figure 2.** (a)–(c) Zonal wavenumber–frequency spectra for 850-hPa zonal wind averaged

1011 over 10°S–10°N in boreal winter after removing the climatological mean seasonal cycle.

1012 Vertical dashed lines represent periods at 80 and 30 days, respectively. (d)–(f) Hovmöller

1013 diagrams of the correlation between the precipitation averaged over 10°S–5°N, 75–100°E

1014 and the intraseasonally filtered precipitation (color) and 850-hPa zonal wind (contour)

1015 averaged over 10°N–10°S. (g)–(i) Zonal wavenumber–frequency power spectra of

1016 anomalous OLR (colors) and phase lag with U850 (vectors) for the symmetric component

1017 of tropical waves, with the vertically upward vector representing a phase lag of 0° with

1018 phase lag increasing clockwise. Three dispersion straight lines with increasing slopes

1019 represent the equatorial Kelvin waves (derived from the shallow water equations)

1020 corresponding to three equivalent depths, 12, 25, and 50 m, respectively. (j)–(l)

1021 Composites of 20–100-day filtered OLR (W m^{-2}, shaded) and 850-hPa wind (m s^{-1},

1022 vector) for MJO phase 5 when deep convection is the strongest over the MC and 850-hPa

1023 wind, with the reference vector (1 m s^{-1}) shown at the top right of each panel, and (m)–

1024 (o) 15°N–15°S averaged p-vertical velocity anomaly (Pa s^{-1}, shaded) and moist static

1025 energy tendency anomaly (W m^{-2}, contour, interval 0.003); solid, dashed, and thick-black

1026 lines represent positive, negative, and zero values, respectively. The number of days used

1027 to generate the composite is shown at the bottom right corner of each panel. (a), (d), (g),

1028 (j), and (m) are from the ERA-Interim and NOAA post-processed data (abbr. ERA-

1029 I/NOAA); (b), (e), (h), (k), and (n) are from the control experiment C–30NS; and (c), (f),

1030 (i), (l), and (o) are from the A–CTL.

1031

1032 **Figure 3.** Evolution of the filtered OLR anomaly (W m^{-2}, shaded) and 850-hPa wind (m

1033 s^{-1}, vector) at phase 2, 4, 6, and 8: (a) the ERA-I/NOAA data, (b) the control coupled

1034 experiment C–30NS, and (c) the uncoupled experiment A–CTL. The unit of the reference

1035 vector shown at the top right corner of each panel is m s^{-1}, and the number of days used

1036 for the composite is shown at the bottom right corner of each panel.

1037

1038 **Figure 4.** (a)–(c) Phase-longitude Hovmöller diagrams of 20–100-day filtered

1039 precipitation (mm day^{-1}, shaded) and SST anomaly (K, contour) averaged over 10°N–

1040 10°S from phase 1 to 8. Contour interval is 0.03; solid, dashed, and thick-black lines

1041 represent positive, negative, and zero values, respectively. (d)–(f) Phase-vertical

1042 Hovmöller diagrams of 20–100-day moisture divergence (shading, 10^{-6} g kg^{-1} s^{-1}) and

1043   zonal wind (contoured, m s^{-1}) averaged over 10°N–10°S, 120–150°E; solid, dashed, and

1044   thick-black curves are positive, negative, and zero values, respectively. (g)–(i) Variation

1045   of 30–60-day filtered precipitation in the eastern IO and the WP in observation (color

1046   shading), and the ratio between intraseasonal and total variance (contoured) and (j)–(l)

1047   composites 20–100-day filtered SST (K, shaded) and 850-hPa winds (m s^{-1}, vector) at

1048   phase 7 when deep convection was the strongest over the dateline. Reference vector

1049   shown at the top right corner of each panel. (a), (d), (g), and (j) are from the ERA-

1050   I/NOAA data; (b), (e), (h), and (k) are from the control coupled experiment C–30NS; and

1051   (c), (f), (i), and (l) are from the uncoupled experiment A–CTL.

1052

1053   **Figure 5.** Composites of 20–100-day filtered oceanic temperature (K, shaded) between 0

1054   and 60 m depth for MJO phase 1, 3, 5, and 7 (shown at the lower right corner of each

1055   panel) in C–30NS, C–LR12m and C–LR34m.

1056

1057   **Figure 6.** (a)–(b) Same as in Fig. 2(a) but for the C–LR12m and C–LR34m. (c)–(d) Same

1058   as in Fig. 2(d) but for the C–LR12m and C–LR34m. (e)–(f) Same as in Fig. 4(a) but for

1059   the C–LR12m and C–LR34m.

1060

1061   **Figure 7.** Same as in Fig. 6 but for the C–HR1mB10m, C–HR1mB30m, and C–

1062   HR1mB60m.

1063

1064   **Figure 8.** Same as in Fig. 6 but for the C–0_30N, C–0_30S, C–30_180E, and C–
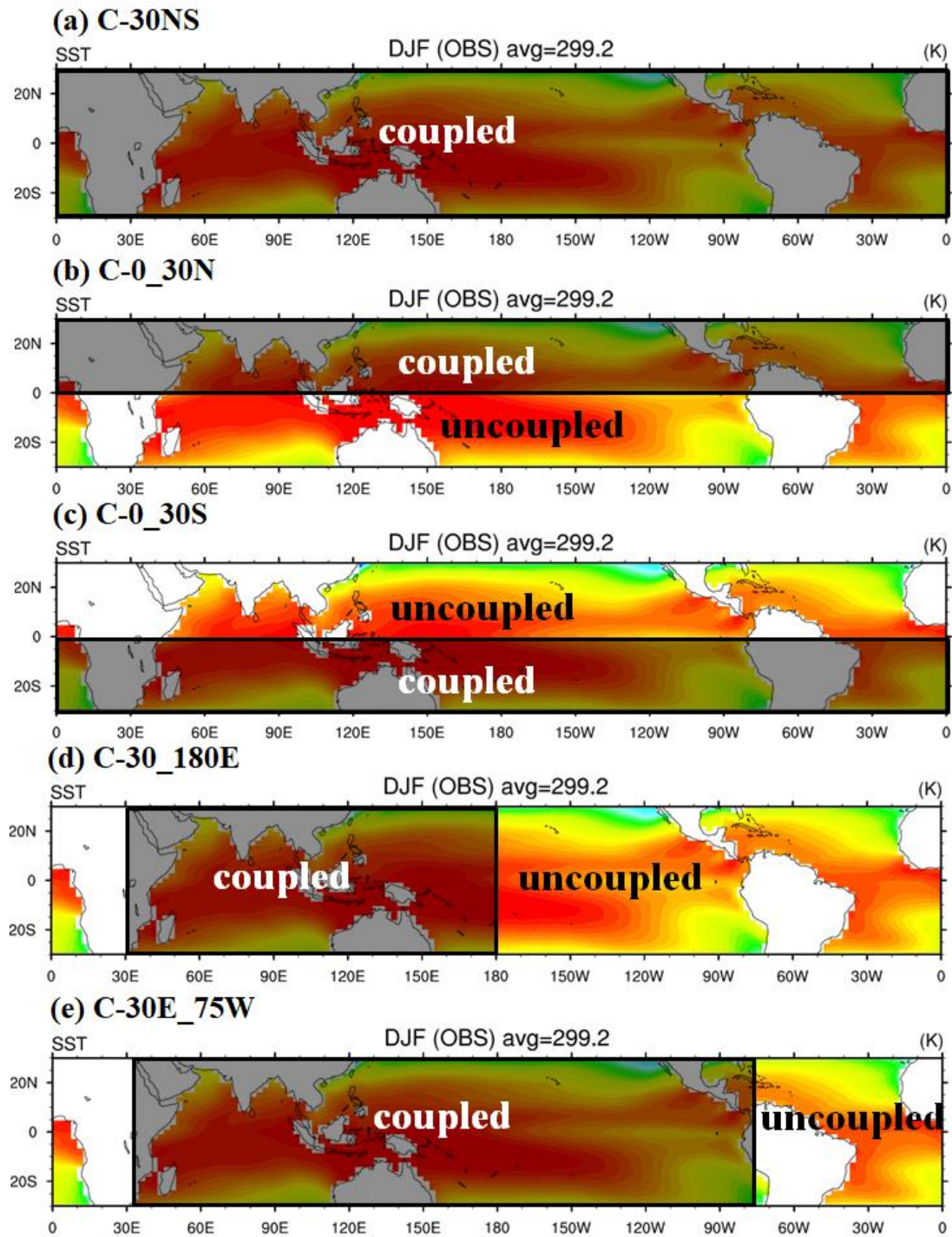
1065   30E_75W.

1066

1067   **Figure 9.** Same as in Fig. 3 but for phase 5 in the C–0_30N, C–0_30S, C–30_180E, and

1068   C–30E_75W.

1069

1070   **Figure 10.** Similar as in Fig. 6 but for the C–30NS–nD.

1071

1072   **Figure 11.** Scattered plots of various MJO indices in the ERA-I/NOAA data and 12

1073   experiments: (a) power ratio of east/west propagating waves of wavenumber 1–3 of 850-

1074   hPa zonal winds (X-axis) with a 30–80-day period and eastward propagation speed of

1075   U850 anomaly (Y-axis) from the Hovmöller diagram and (b) RMM1 and RMM2 variance

1076   and eastward propagation speed of the filtered precipitation anomaly derived from the

1077   Hovmöller diagram.

Figure 1. Schematics of coupled and uncoupled domains in the regional coupling experiment: (a) C–30NS, (b) C–0_30N, (c) C–0_30S, (d) C–30_180E, and (e) C–30E_75W. The background is the climatological mean SST in December–February (DJF).

1083
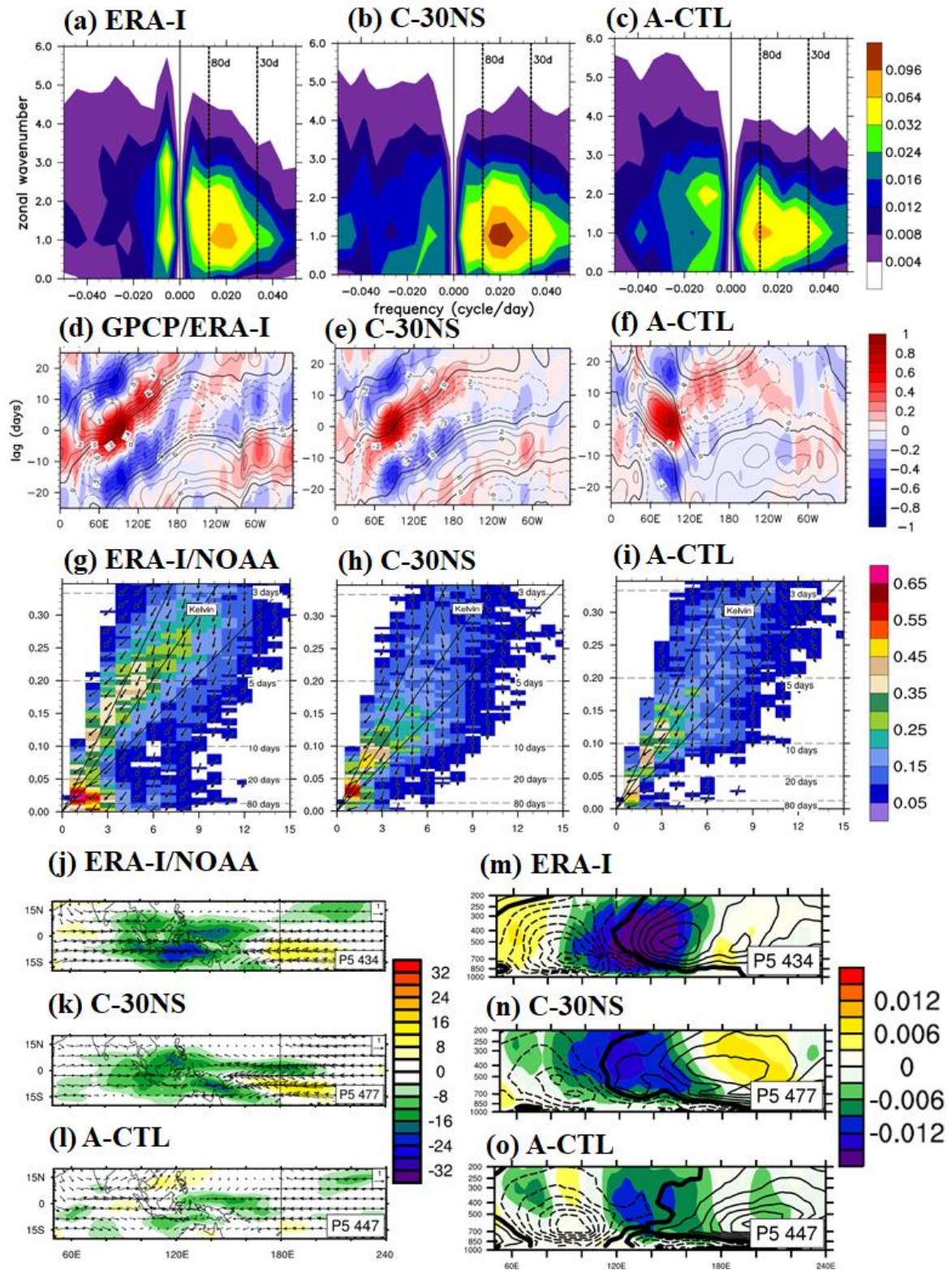
Figure 2. (a)–(c) Zonal wavenumber–frequency spectra for 850-hPa zonal wind averaged over 10°S–10°N in boreal winter after removing the climatological mean seasonal cycle. Vertical dashed lines represent periods at 80 and 30 days, respectively. (d)–(f) Hovmöller

1084
1085
1086
1087
1088

1089   diagrams of the correlation between the precipitation averaged over 10°S–5°N, 75–100°E
1090   and the intraseasonally filtered precipitation (color) and 850-hPa zonal wind (contour)
1091   averaged over 10°N–10°S. (g)–(i) Zonal wavenumber–frequency power spectra of
1092   anomalous OLR (colors) and phase lag with U850 (vectors) for the symmetric component
1093   of tropical waves, with the vertically upward vector representing a phase lag of 0° with
1094   phase lag increasing clockwise. Three dispersion straight lines with increasing slopes
1095   represent the equatorial Kelvin waves (derived from the shallow water equations)
1096   corresponding to three equivalent depths, 12, 25, and 50 m, respectively. (j)–(l)
1097   Composites of 20–100-day filtered OLR (W m^{-2}, shaded) and 850-hPa wind (m s^{-1},
1098   vector) for MJO phase 5 when deep convection is the strongest over the MC and 850 hPa
1099   wind, with the reference vector (1 m s^{-1}) shown at the top right of each panel, and (m)–
1100   (o) 15°N–15°S averaged p-vertical velocity anomaly (Pa s^{-1}, shaded) and moist static
1101   energy tendency anomaly (W m^{-2}, contour, interval 0.003); solid, dashed, and thick-black
1102   lines represent positive, negative, and zero values, respectively. The number of days used
1103   to generate the composite is shown at the bottom right corner of each panel. (a), (d), (g),
1104   (j), and (m) are from the ERA-Interim and NOAA post-processed data (abbr. ERA-
1105   I/NOAA); (b), (e), (h), (k), and (n) are from the control experiment C–30NS; and (c), (f),
1106   (i), (l), and (o) are from the A–CTL.

1107
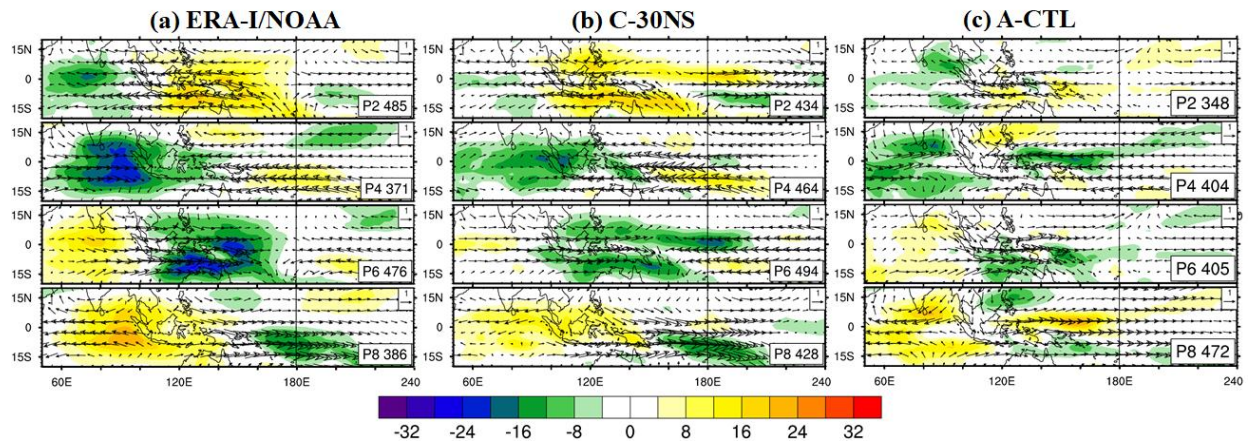
1108

1109

1110 **Figure 3.** Evolution of the filtered OLR anomaly (W m^{-2}, shaded) and 850-hPa wind (m
1111 s^{-1}, vector) at phase 2, 4, 6, and 8: (a) the ERA-I/NOAA data, (b) the control coupled
1112 experiment C–30NS, and (c) the uncoupled experiment A–CTL. The unit of the reference
1113 vector shown at the top right corner of each panel is m s^{-1}, and the number of days used
1114 for the composite is shown at the bottom right corner of each panel.
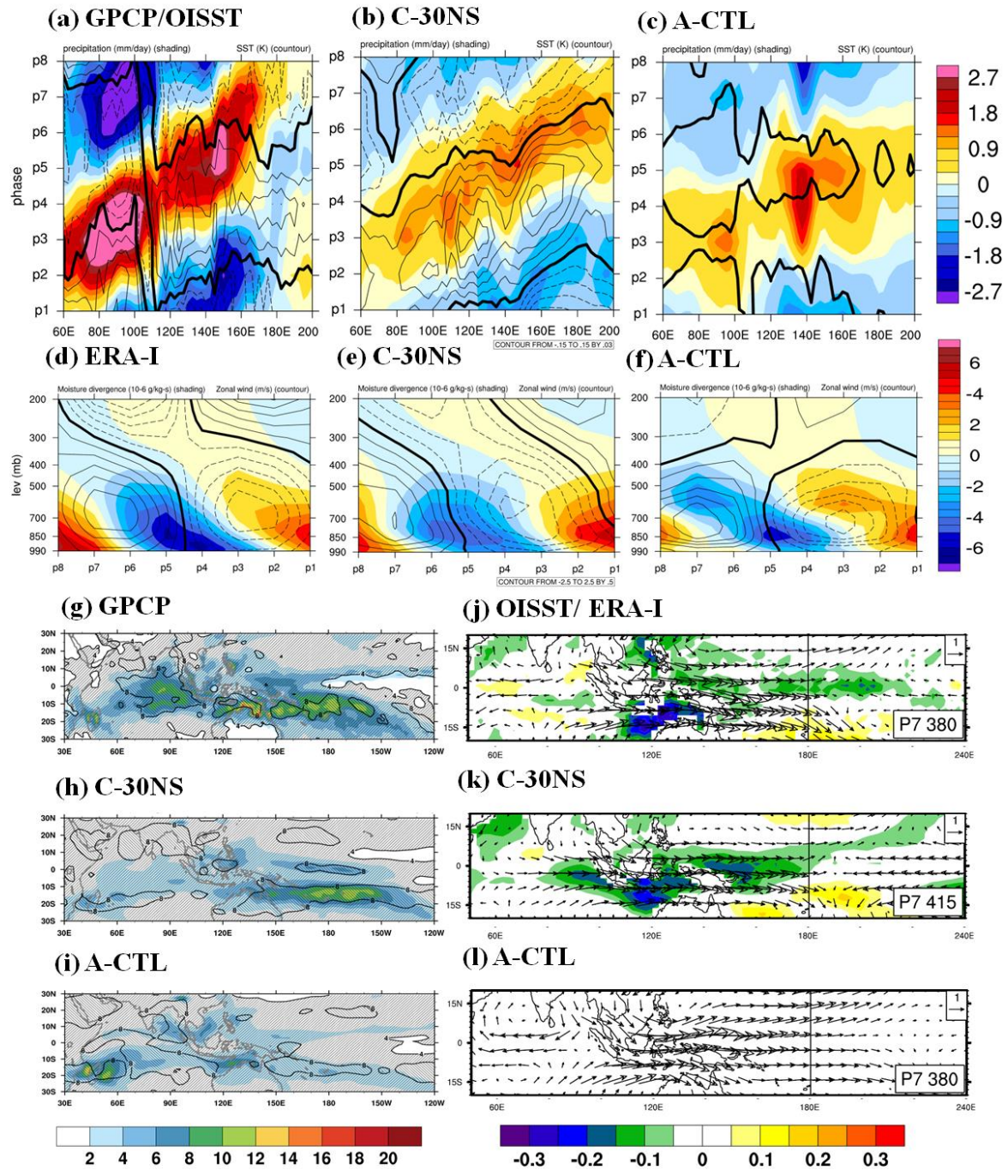
Figure 4. (a)–(c) Phase-longitude Hovmöller diagrams of 20–100-day filtered precipitation (mm day^{-1}, shaded) and SST anomaly (K, contour) averaged over 10°N–10°S from phase 1 to 8. Contour interval is 0.03; solid, dashed, and thick-black lines represent positive, negative, and zero values, respectively. (d)–(f) Phase-vertical Hovmöller diagrams of 20–100-day moisture divergence (shading, 10^{-6} g kg^{-1} s^{-1}) and zonal wind (contoured, m s^{-1}) averaged over 10°N–10°S, 120–150°E; solid, dashed, and thick-black curves are positive, negative, and zero values, respectively. (g)–(i) Variation of 30–60-day filtered precipitation in the eastern IO and the WP in observation (color

1125 shading), and the ratio between intraseasonal and total variance (contoured) and (j)–(l)

1126 composites 20–100-day filtered SST (K, shaded) and 850-hPa winds (m s^{-1}, vector) at

1127 phase 7 when deep convection was the strongest over the dateline. Reference vector

1128 shown at the top right corner of each panel. (a), (d), (g), and (j) are from the ERA-

1129 I/NOAA data; (b), (e), (h), and (k) are from the control coupled experiment C–30NS; and

1130 (c), (f), (i), and (l) are from the uncoupled experiment A–CTL.

1131
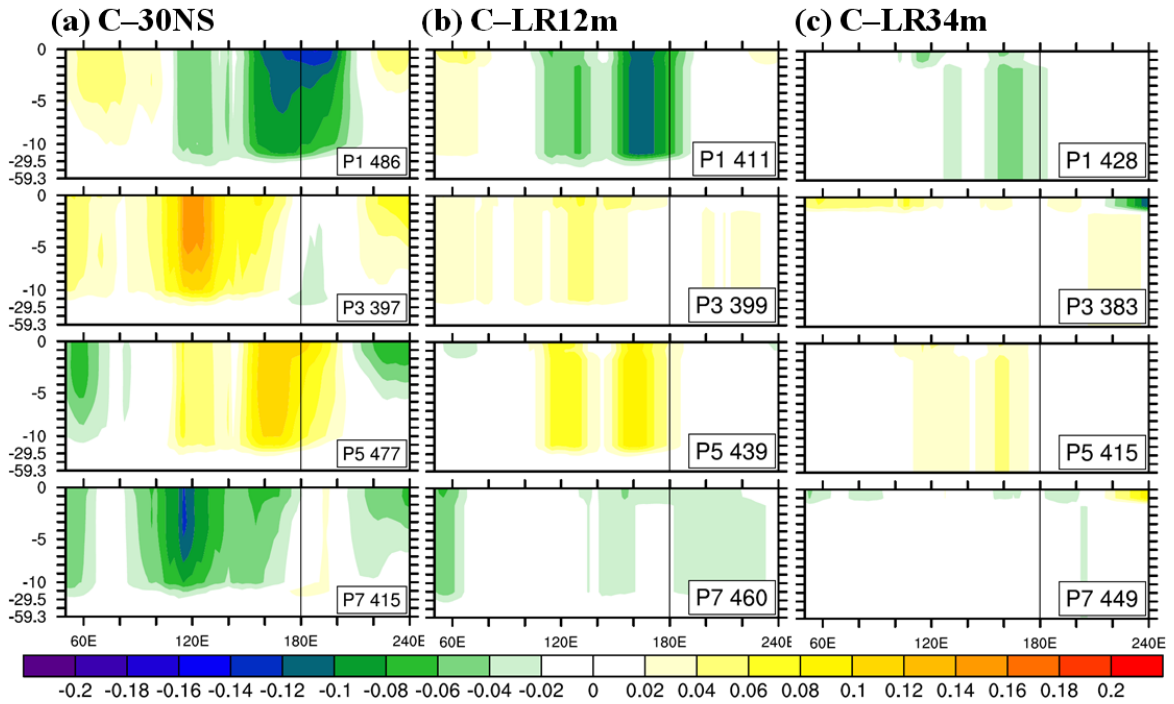
Figure 5. Composites of 20–100-day filtered oceanic temperature (K, shaded) between 0 and 60 m depth for MJO phase 1, 3, 5, and 7 (shown at the lower right corner of each panel) in C–30NS, C–LR12m and C–LR34m.
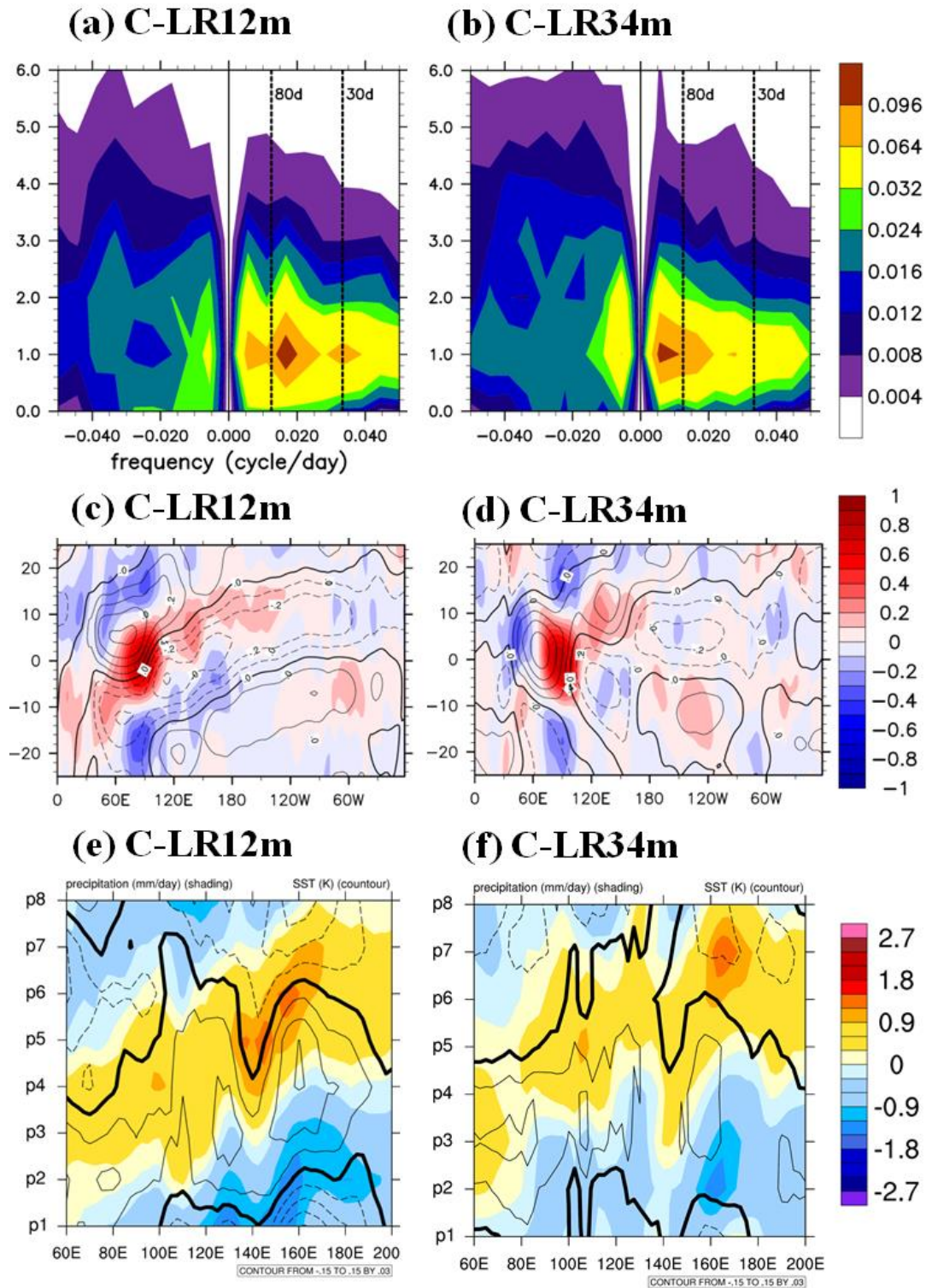
Figure 6. (a)–(b) Same as in Fig. 2(a) but for the C–LR12m and C–LR34m. (c)–(d) Same as in Fig. 2(d) but for the C–LR12m and C–LR34m. (e)–(f) Same as in Fig. 4(a) but for the C–LR12m and C–LR34m.
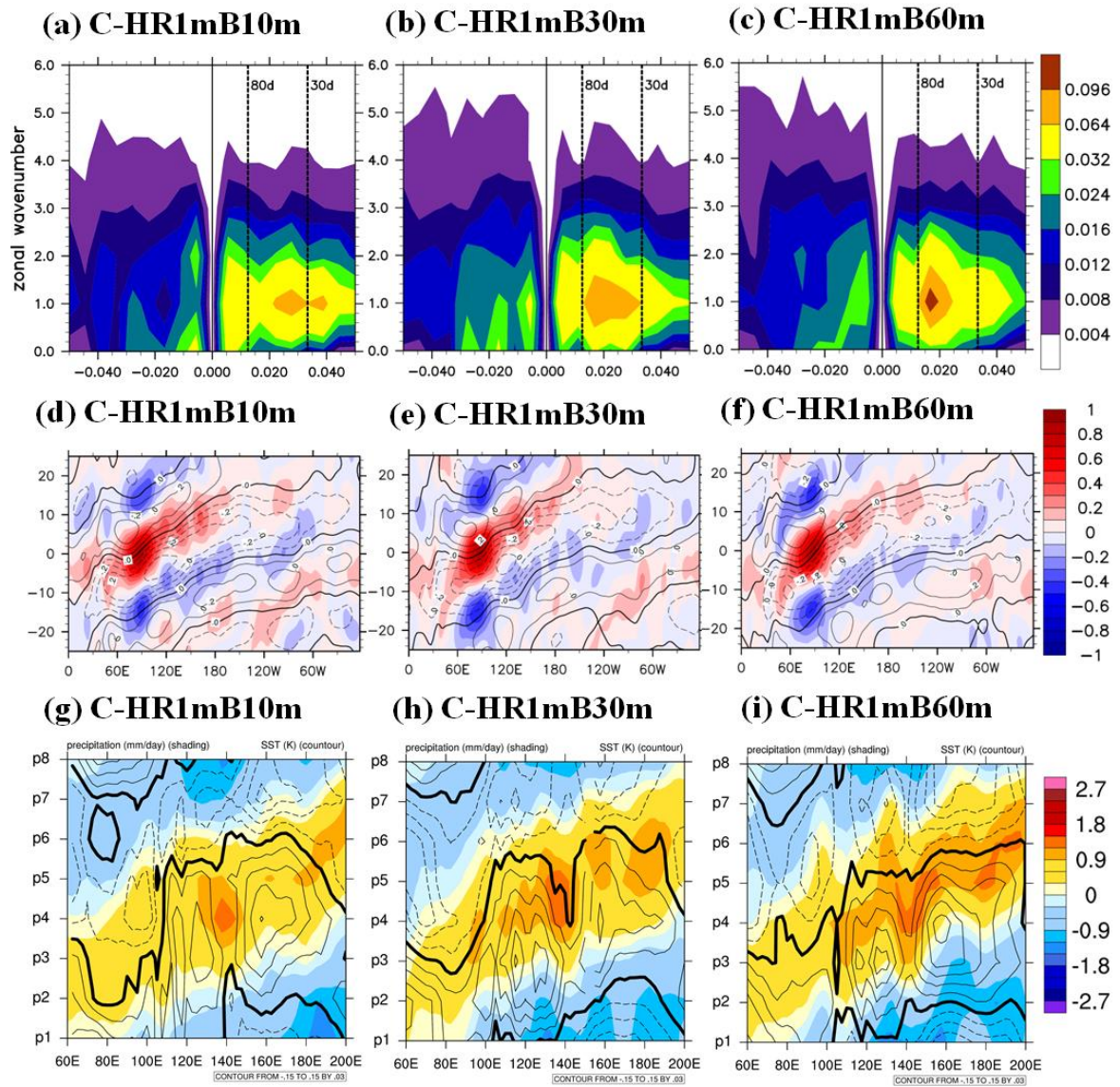
Figure 7. Same as in Fig. 6 but for the C–HR1mB10m, C–HR1mB30m, and C–HR1mB60m.
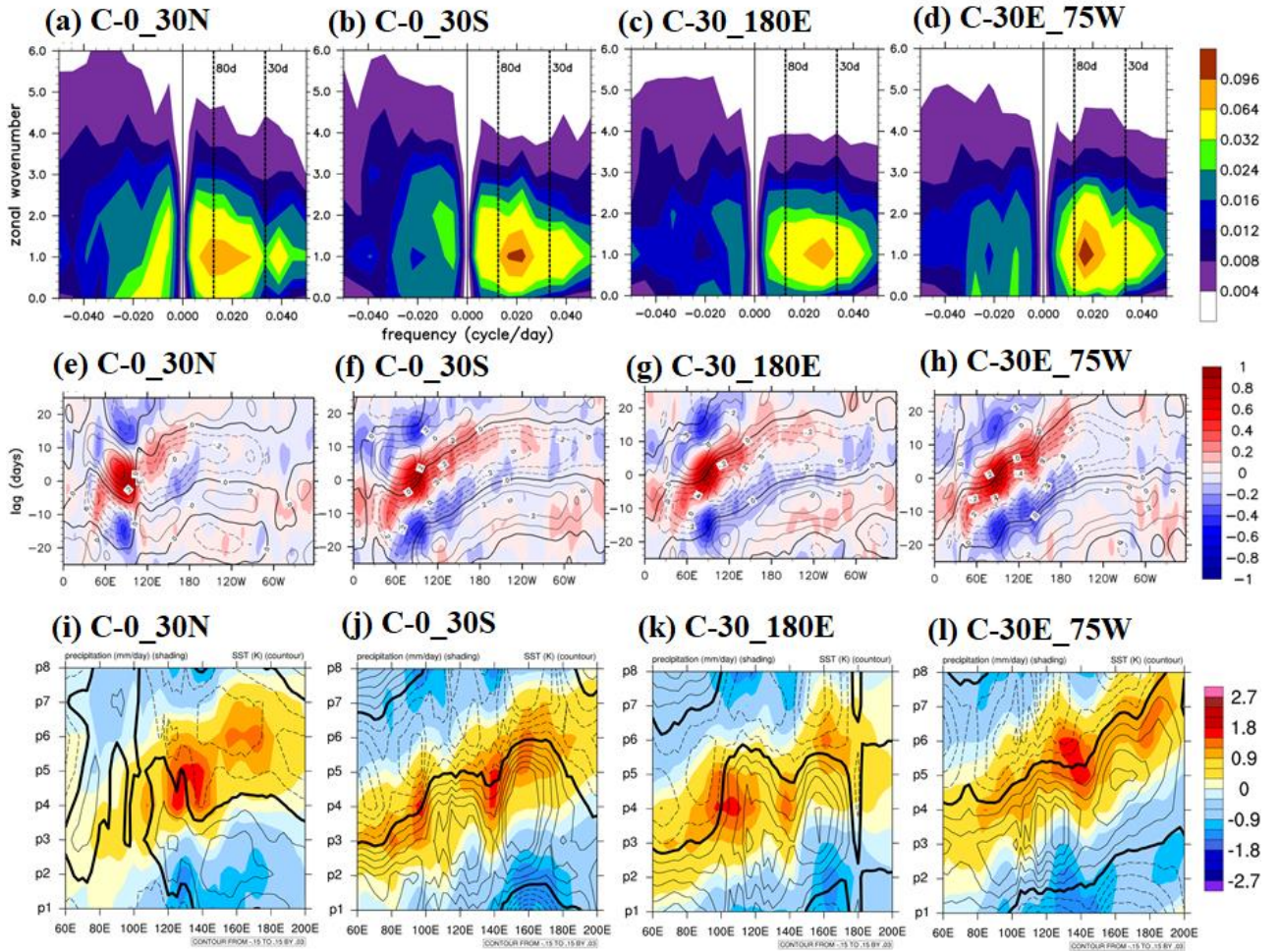
1147

1148

1149 **Figure 8.** Same as in Fig. 6 but for the C–0_30N, C–0_30S, C–30_180E, and C–

1150 30E_75W.
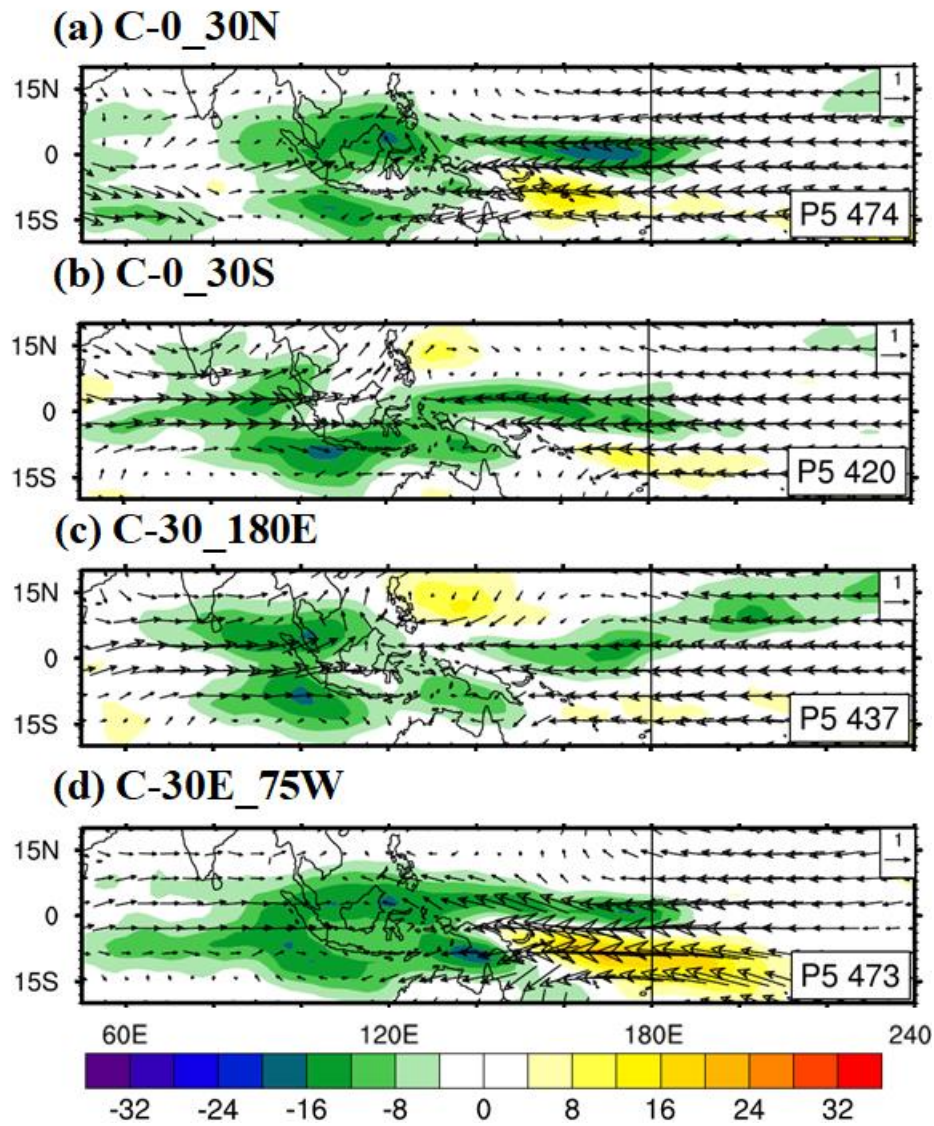
(a) C-0_30N

(b) C-0_30S

(c) C-30_180E

(d) C-30E_75W

Figure 9. Same as in Fig. 3 but for phase 5 in the C–0_30N, C–0_30S, C–30_180E, and C–30E_75W.
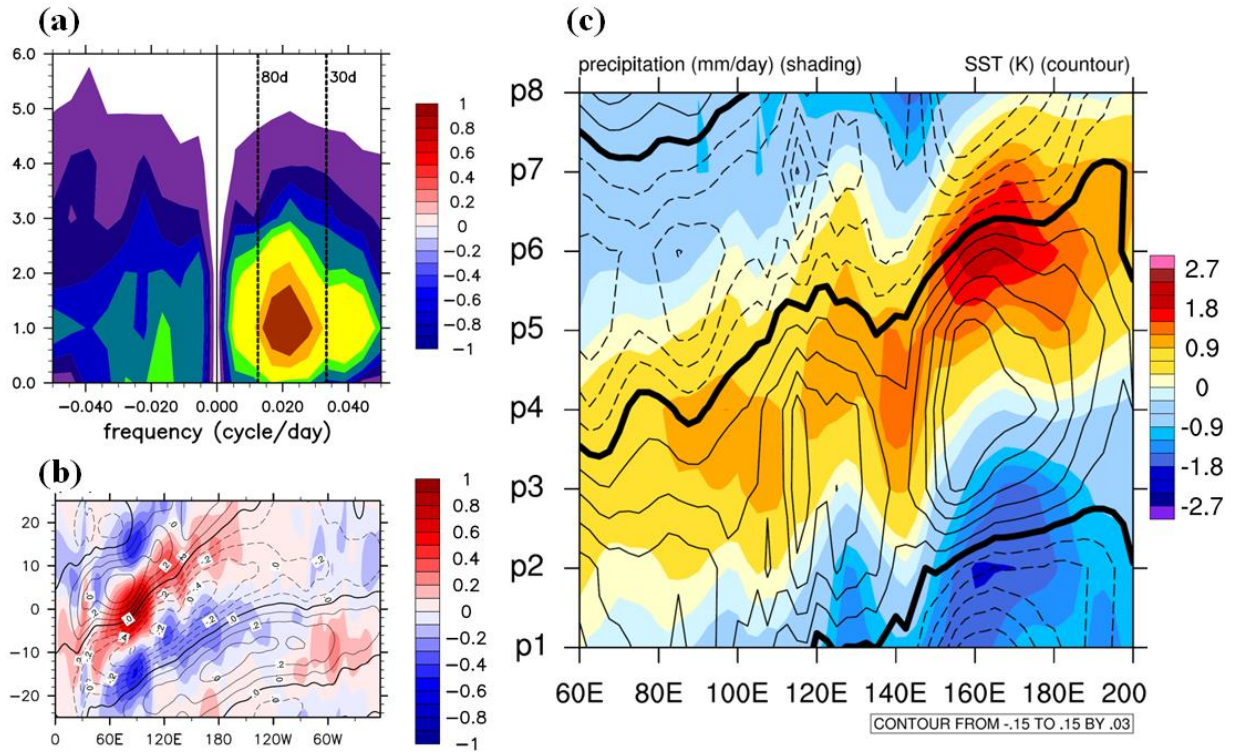
1155
1156

1157   **Figure 10.** Similar as in Fig. 6 but for the C–30NS–nD.
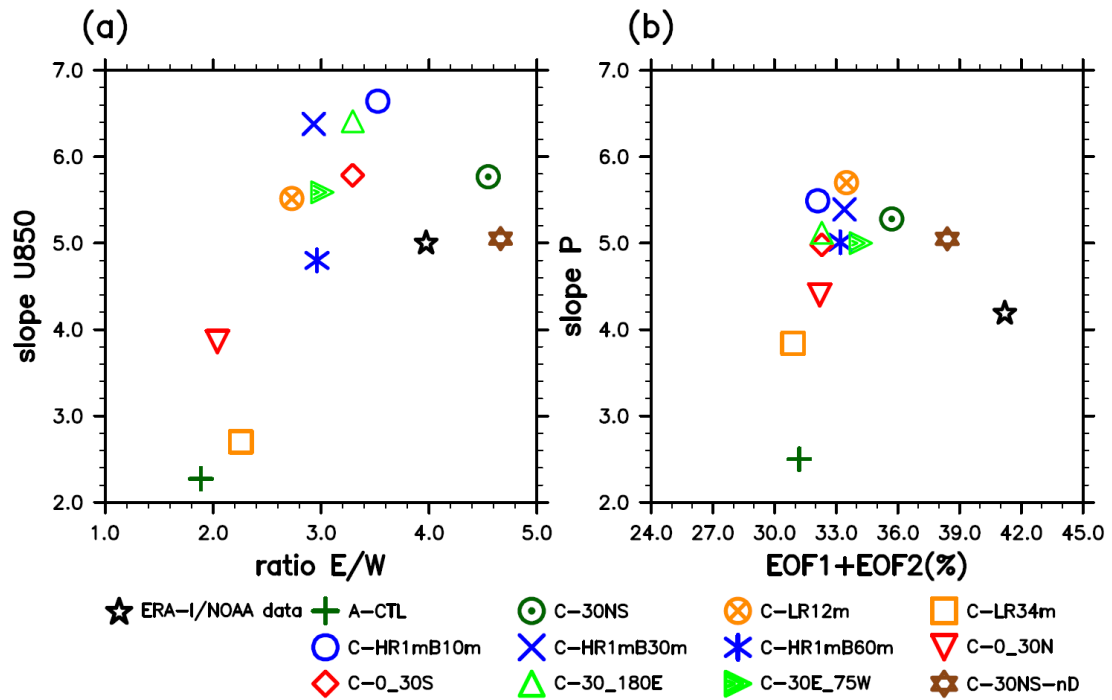
Figure 11. Scattered plots of various MJO indices in the ERA-I/NOAA data and 12 experiments: (a) power ratio of east/west propagating waves of wavenumber 1–3 of 850-hPa zonal winds (X-axis) with a 30–80-day period and eastward propagation speed of U850 anomaly (Y-axis) from the Hovmöller diagram and (b) RMM1 and RMM2 variance and eastward propagation speed of the filtered precipitation anomaly derived from the Hovmöller diagram.

1167 **Appendix: 1-D high-resolution TKE ocean model**

1168   The 1-D high-resolution turbulence kinetic energy ocean model SIT was used to

1169 simulate the diurnal fluctuation of SST and surface energy fluxes. The model was well

1170 verified against surface and subsurface observations in the South China Sea (Lan et al.,

1171 2010) and the tropical WP (Tu and Tsuang, 2005). Variations in sea water temperature (T),

1172 current ($\vec{u}$), and salinity (S) were determined (Gaspar et al., 1990) using the following

1173 equations.

1174
$$\frac{\partial T}{\partial t} = (k_h + v_h)\frac{\partial^2 T}{\partial z^2} + \frac{R_{sn}}{\rho_{w0}c_w}\frac{\partial F}{\partial z} \tag{1}$$

1175
$$\frac{\partial \vec{u}}{\partial t} = -f\,\hat{k} \times \vec{u} + (k_m + v_m)\frac{\partial^2 \vec{u}}{\partial z^2} \tag{2}$$

1176
$$\frac{\partial S}{\partial t} = (k_h + v_h)\frac{\partial^2 S}{\partial z^2} \tag{3}$$

1177 where R_{sn} is the net solar radiation at the surface (W m^{-2}), $F(z)$ is the fraction

1178 (dimensionless) of R_{sn} that penetrates to the depth z, and k_h and k_m are eddy diffusion

1179 coefficients for heat and momentum (m^2 s^{-1}), respectively. The value of k_h within the cool

1180 skin layer and that of k_m within the viscous layer were set to zero. Molecular transport is

1181 the only mechanism for the vertical diffusion of heat and momentum in the cool skin and

1182 viscous layer, respectively (Hasse, 1971; Grassl, 1976; Wu, 1985).The parameters v_m

1183 and v_h are the molecular diffusion coefficients for momentum and temperature,

1184 respectively, ρ_{w0} is the density (kg m^{-3}) of water, and c_w is the specific heat capacity of

1185 water at constant pressure (J kg^{-1} K^{-1}). S is salinity (‰), $\vec{u}$ is the current velocity (m s^{-1}),

1186 f is the Coriolis parameter (dimensionless), and $\hat{k}$ is the vertical unit vector (m s^{-1}).

1187   Using the numerical solution of the surface layer (T_0), we disregard the time-term of

1188 the 2-metre air temperature (T_{2m}), which can be considered the upper boundary of an

1189 ocean, as well as the numerical solution of the surface long-wave radiation T_0 term and

1190 aerodynamic resistance (r_a).

$$\frac{\partial T_0}{\partial t} = \frac{G_0}{\rho_w \cdot c_w \cdot h_e} + \frac{R_{sn}[F(z_0) - F(z_0 - d)]}{\rho_w \cdot c_w \cdot h_e} - \frac{G_{0,1}}{\rho_w \cdot c_w \cdot h_e}$$

$$= \frac{R_{ld} - R_{lu} - H - LE}{\rho_w \cdot c_w \cdot h_e} + \frac{R_{sn}[F(z_0) - F(z_0 - d)]}{\rho_w \cdot c_w \cdot h_e} - k_0 \frac{T_0 - T_1}{h_e(z_0 - z_1)}$$

$$= \frac{1}{\rho_w \cdot c_w \cdot h_e}[R_{ld} - \varepsilon\sigma T_0^4 - \frac{\rho_a c_a (T_0 - T_{2m})}{r_a} - \frac{\rho_a L_v (q^*(T_0) - q_a)}{r_a}] \qquad (3)$$

$$+ \frac{R_{sn}[F(z_0) - F(z_0 - d)]}{\rho_w \cdot c_w \cdot h_e} - k_0 \frac{T_0 - T_1}{h_e(z_0 - z_1)}$$

1192   where G_0 is the net flux of the ocean surface, $G_{0,1}$ is the net flux in the bottom depth of T_0

1193   grid, and K_0 and h_e are eddy diffusion coefficients and the effective thickness of T_0 layer,

1194   respectively. c_a is the specific heat capacity of surface air at constant pressure (J kg^{-1} K^{-1}).

1195 L_v is the latent heat of evaporation of water q. We use finite difference approximation to

1196   divide time-term into j+1 and j.

$$\frac{T_0^{j+1} - T_0^j}{\Delta t} = \frac{1}{\rho_w \cdot c_w \cdot h_e}\{R_{ld} - \varepsilon\sigma(T_0^j)^4 - \frac{\rho_a c_a}{r_a}[\beta T_0^{j+1} + (1-\beta)T_0^j - T_{2m}^j]$$

$$- \frac{\rho_a L_v (q^*(T_0) - q_a)}{r_a}\} + \frac{R_{sn}[F(z_0) - F(z_0 - d)]}{\rho_w \cdot c_w \cdot h_e} \qquad (4)$$

$$- \frac{k_0}{h_e(z_0 - z_1)}[(\beta T_0^{j+1} + (1-\beta)T_0^j) - (\beta T_1^{j+1} + (1-\beta)T_1^j)]$$

$$(1 + \frac{\Delta t}{\rho_w \cdot c_w \cdot h_e}\frac{\rho_a c_a}{r_a}\beta + \frac{k_0 \cdot \Delta t}{h_e(z_0 - z_1)}\beta)T_0^{j+1} - \frac{k_0 \cdot \Delta t}{h_e(z_0 - z_1)}\beta T_1^{j+1}$$

$$= T_0^j + \frac{\Delta t}{\rho_w \cdot c_w \cdot h_e}[R_{ld} - \frac{\rho_a L_v (q^*(T_0) - q_a)}{r_a}] + \Delta t \frac{R_{sn}[F(z_0) - F(z_0 - d)]}{\rho_w \cdot c_w \cdot h_e}$$

$$+ (1-\beta)(\frac{\Delta t}{\rho_w \cdot c_w \cdot h_e} + \frac{\rho_a c_a}{r_a} + \frac{k_0 \cdot \Delta t}{h_e(z_0 - z_1)})T_0^j - \frac{\Delta t}{\rho_w \cdot c_w \cdot h_e}\varepsilon\sigma(T_0^j)^4$$

$$+ \frac{k_0 \cdot \Delta t}{h_e(z_0 - z_1)}(1-\beta)T_1^j \qquad (5)$$

$$= T_0^j + \frac{\Delta t}{\rho_w \cdot c_w \cdot h_e}[R_{ld} - \frac{\rho_a L_v (q^*(T_0) - q_a)}{r_a} - \varepsilon\sigma(T_0^j)^4]$$

$$+ \Delta t \frac{R_{sn}[F(z_0) - F(z_0 - d)]}{\rho_w \cdot c_w \cdot h_e} - (1-\beta)(\frac{\Delta t}{\rho_w \cdot c_w \cdot h_e} + \frac{\rho_a c_a}{r_a} + y_0)T_0^j$$

$$- (1-\beta)y_0(T_0^j - T_1^j)$$

1199   Since the T_1 is next temperature below the T_0, the numerical solution is based on the

53

1200   average temperature of the h_1 layer, $h_1 = z_0 - 0.5(z_1 + z_2)$. The parameter β controls the

1201   time scheme (i.e., 1 controls a backward time scheme, 0.5 controls a Crank-Nicolson

1202   method, and 0 controls a forward time scheme).

$$\frac{\partial T_1}{\partial t} = \frac{G_0 + G_{1,2}}{\rho_w \cdot c_w \cdot h_1} + \frac{R_{sn}[F(z_0) - F(\frac{z_1 + z_2}{2})]}{\rho_w \cdot c_w \cdot h_1}$$

$$= \frac{h_e}{h_1}\frac{\partial T_0}{\partial t} + k_0\frac{T_0 - T_1}{h_1(z_0 - z_1)} + \frac{R_{sn}[F(z_0) - F(\frac{z_1 + z_2}{2})]}{\rho_w \cdot c_w \cdot h_1} - k_1\frac{T_1 - T_2}{h_1(z_1 - z_2)}$$

1203

$$\frac{T_1^{j+1} - T_1^{j}}{\Delta t} = \frac{h_e}{h_1}\frac{T_0^{j+1} - T_0^{j}}{\Delta t} + k_0\frac{[\beta T_0^{j+1} + (1-\beta)T_0^{j}] - [\beta T_1^{j+1} + (1-\beta)T_1^{j}]}{h_1(z_0 - z_1)}$$ (6)

$$+ \frac{R_{sn}[F(z_0 - d) - F(\frac{z_1 + z_2}{2})]}{\rho_w \cdot c_w \cdot h_1} - \frac{k_1}{h_1(z_1 - z_2)}[(\beta T_1^{j+1} + (1-\beta)T_1^{j})$$

$$- (\beta T_2^{j+1} + (1-\beta)T_2^{j})]$$

1204   Specifically, the numerical solution of the next T_2 below the T_1 is not affected by the G_0

1205   term, and that of the energy term is mainly affected by the $G_{1,2}$, $G_{2,3}$, and R_{sn} components.

$$\frac{\partial T_2}{\partial t} = \frac{-G_{1,2} + G_{2,3}}{\rho_w \cdot c_w \cdot h_2} + \frac{R_{sn}[F(\frac{z_1 + z_2}{2}) - F(\frac{z_2 + z_3}{2})]}{\rho_w \cdot c_w \cdot h_2}$$

$$= \frac{R_{sn}[F(\frac{z_1 + z_2}{2}) - F(\frac{z_2 + z_3}{2})]}{\rho_w \cdot c_w \cdot h_2} + k_1\frac{T_1 - T_2}{h_2(z_1 - z_2)} - k_2\frac{T_2 - T_3}{h_2(z_2 - z_3)}$$

1206

$$\frac{T_2^{j+1} - T_2^{j}}{\Delta t} = \frac{R_{sn}[F(\frac{z_1 + z_2}{2}) - F(\frac{z_2 + z_3}{2})]}{\rho_w \cdot c_w \cdot h_2} + k_1\frac{[\beta T_1^{j+1} + (1-\beta)T_1^{j}] - [\beta T_2^{j+1} + (1-\beta)T_2^{j}]}{h_2(z_1 - z_2)}$$ (7)

$$- k_2\frac{[\beta T_2^{j+1} + (1-\beta)T_2^{j}] - [\beta T_3^{j+1} + (1-\beta)T_3^{j}]}{h_2(z_1 - z_2)}$$

1207   Similarly, the numerical solutions of layers between 3 and 41 are as follows:

$$(-\beta x_k)T_{k-1}^{j+1} + (1 + \beta \cdot x_k + \beta \cdot y_k)T_2^{j+1} - \beta \cdot y_k T_{k+1}^{j+1}$$

1208

$$= T_k^{j} + \frac{\Delta t \cdot R_{sn}}{\rho_w \cdot c_w \cdot h_k}\{R_{sn}[F(\frac{z_{k-1} + z_k}{2}) - F(\frac{z_k + z_{k+1}}{2})]\} + (1-\beta)[x_k(T_{k-1}^{j} - T_k^{j})$$ (8)

$$- y_2(T_k^{j} - T_{k+1}^{j})]$$

1209   where $y_0 = \dfrac{\Delta t}{h_e} \dfrac{k_0}{z_0 - z_1}$

1210 $x_k = \dfrac{\Delta t}{h_k} \left(\dfrac{k_{k-1}}{k_{k-1} - k_k} \right) \quad for \quad k = 1, n$

1211 $y_k = \dfrac{\Delta t}{h_k} \left(\dfrac{k_k}{k_k - k_{k+1}} \right) \quad for \quad k = 1, n$

1212 $x_g = \dfrac{\Delta t \cdot \rho_w \cdot c_w}{\rho_g \cdot c_g \sqrt{\dfrac{k_g}{w}}} \left(\dfrac{k_n}{z_n - z_g} \right)$

1213   Finally, we get a triangular matrix for numerical solutions of 1-D high-resolution

1214   turbulence kinetic energy ocean model SIT.

$$
\begin{bmatrix}
1+\beta\dfrac{\Delta t}{\rho_w c_w h_e}\dfrac{\rho_a c_a}{r_a}+y_0\beta & -\beta y_0 & & & & \\
-\beta x_1-\dfrac{h_e}{h_1} & 1+\beta x_1+\beta y_1 & -\beta y_1 & & & \\
& & & & & \\
& & -\beta x_k & 1+\beta x_k+\beta y_k & -\beta y_k & \\
& & & & & \\
& & & & -\beta x_g & 1+\beta x_g
\end{bmatrix}
\begin{bmatrix}
T_0^{j+1} \\ T_1^{j+1} \\ \\ T_{k-1}^{j+1} \\ T_k^{j+1} \\ T_{k+1}^{j+1} \\ \\ T_n^{j+1} \\ T_g^{j+1}
\end{bmatrix} =
$$

$$
\begin{bmatrix}
T_0^j + \dfrac{\Delta t \cdot R_{sn}[F(z_0)-F(z_0-d)]}{\rho_w c_w h_e} + \dfrac{\Delta t}{\rho_w c_w h_e}[R_{ld}-\dfrac{\rho_a L_v(q^*(T_0^j)-q_a)}{r_a}-\varepsilon\sigma(T_0^j)^4]-(1-\beta)[(\dfrac{\Delta t}{\rho_w c_w h_e}\dfrac{\rho_a c_a}{r_a}+y_0)T_0^j+y_0(T_0^j-T_1^j)] \\
T_1^j - \dfrac{h_e}{h_1}T_0^j + \dfrac{\Delta t \cdot R_{sn}}{\rho_w c_w h_1}\left[F(z_0-d)-F\left(\dfrac{z_1+z_2}{2}\right)\right]+(1-\beta)[x_1(T_0^j-T_1^j)-y_1(T_1^j-T_2^j)] \\
\\
T_k^j + \dfrac{\Delta t \cdot R_{sn}}{\rho_w c_w h_k}\left[F\left(\dfrac{z_{k-1}+z_k}{2}\right)-F\left(\dfrac{z_k+z_{k+1}}{2}\right)\right]+(1-\beta)[x_k(T_{k-1}^j-T_k^j)-y_k(T_k^j-T_{k+1}^j)] \\
\\
T_g^j + \dfrac{\Delta t R_{sn}F(z_g)}{\rho_g c_g \sqrt{\dfrac{k_g}{\omega}}} + (1-\beta)x_g(T_n^j-T_g^j)
\end{bmatrix}
$$

1215

1216   The eddy diffusivity for momentum k_m is simulated using an eddy kinetic energy

1217   approach based on the Prandtl–Kolmogorov hypothesis as follows:

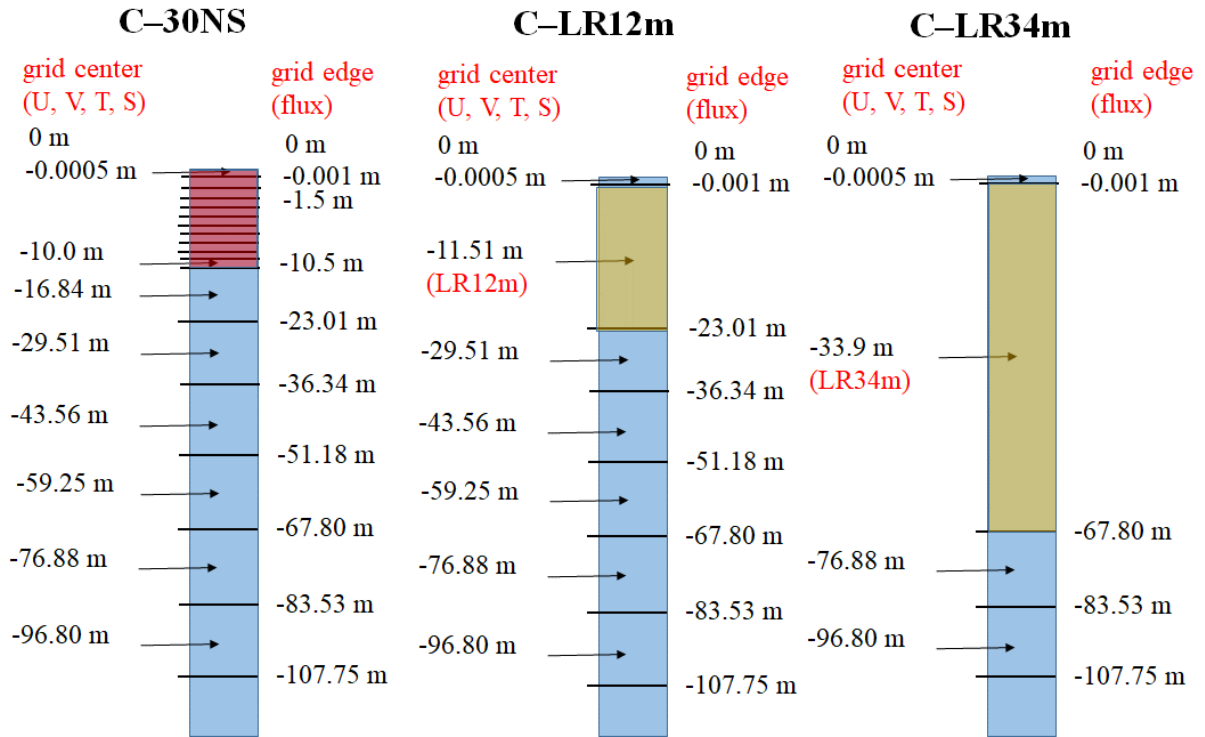1218 $k_m = c_k l_k \sqrt{E}$ $\qquad\qquad\qquad\qquad\qquad$ (9)

1219 where $c_k = 0.1$ (Gaspar et al., 1990), l_k is the mixing length (m), and

1220 $E = 0.5(u'^2 + v'^2 + w'^2)$ is turbulent kinetic energy. The turbulent kinetic energy (E) is

1221 determined using a 1-D equation (Mellor and Yamada, 1982) as follows:

$$\frac{\partial E}{\partial t} = \frac{\partial}{\partial z} k_m \frac{\partial E}{\partial z} + k_m \left(\frac{\partial \bar{u}}{\partial z}\right)^2 + k_h \frac{g}{\rho_w} \frac{\partial \rho_w}{\partial z} - c_\varepsilon \frac{E^{3/2}}{l_\varepsilon} \tag{10}$$

1223 where $c_\varepsilon = 0.7$ (Gaspar et al., 1990), g is the gravity (m s^{-2}), ρ_w is the density of water

1224 (kg m^{-3}), and l_ε is the characteristic dissipation length (m). The mixing length (l_k) and

1225 dissipation length (l_ε) were determined following the approach reported by Gaspar et al.

1226 (1990). This approach is valid for determining the eddy diffusivity of both the ocean

1227 mixed layer and surface layer.

1228 In the SIT model setting, the specific heat of sea water is a constant (4186.84 J kg^{-1}

1229 K^{-1}), and the Prandtl number in water is defined as the ratio of momentum diffusivity to

1230 thermal diffusivity, which is a dimensionless number set as a constant (1.0). The

1231 kinematic viscosity is a constant (1.14 $\times$ 10^{-6} m^2 s^{-1}; Paulson and Simpson, 1981), and

1232 the downward solar radiative flux into water with nine wavelength bands was determined

1233 following the approach reported by Paulson and Simpson (1981). The minimum turbulent

1234 kinetic energy is set to 10^{-6} m^2 s^{-2}, and the zero displacement is set to 0.03 m.

1235 The resolution in the upper 10.5 m is considerably fine to capture the upper-ocean

1236 warm layer, and the thickness of the first layer below sea surface is 0.05 mm to reproduce

1237 the ocean surface cool skin. The vertical grid within 107.8 m in C–30NS, C–LR12m and

1238 C–LR34m as Fig. A1. Besides SST cool skin layer, C–LR12m and C–LR34m have a first

1239 layer with grid center of -11.5 m and -33.9 m, respectively. In lowest boundary

1240 experiment, the total vertically-gridded layers in C–HR1mB10m, C–HR1mB30m and C–

1241 HR1mB60m are showed as Fig. A2.

C–30NS

grid center (U, V, T, S)
grid edge (flux)

0 m — 0 m
-0.0005 m — -0.001 m
-1.5 m
-10.0 m — -10.5 m
-16.84 m
-23.01 m
-29.51 m
-36.34 m
-43.56 m
-51.18 m
-59.25 m
-67.80 m
-76.88 m
-83.53 m
-96.80 m
-107.75 m

C–LR12m

grid center (U, V, T, S)
grid edge (flux)

0 m — 0 m
-0.0005 m — -0.001 m
-11.51 m (LR12m)
-23.01 m
-29.51 m
-36.34 m
-43.56 m
-51.18 m
-59.25 m
-67.80 m
-76.88 m
-83.53 m
-96.80 m
-107.75 m

C–LR34m

grid center (U, V, T, S)
grid edge (flux)

0 m — 0 m
-0.0005 m — -0.001 m
-33.9 m (LR34m)
-67.80 m
-76.88 m — -83.53 m
-96.80 m — -107.75 m

1242

1243

1244 Figure A1. Diagram showing the vertical grid within 107.8 m in C–30NS, C–LR12m and

1245 C–LR34m, the model is as thick as 107.8 meters and with several layers between surface

1246 and model bottom. C–LR12m (31 vertical layers) and C–LR34m (28 vertical layers) have

1247 a first layer with grid center of 12 m and 34 m, respectively, but have the same vertical

1248 discretization as in the control experiment (C–30NS, 41 vertical layers) below the first

1249 layer.

1250
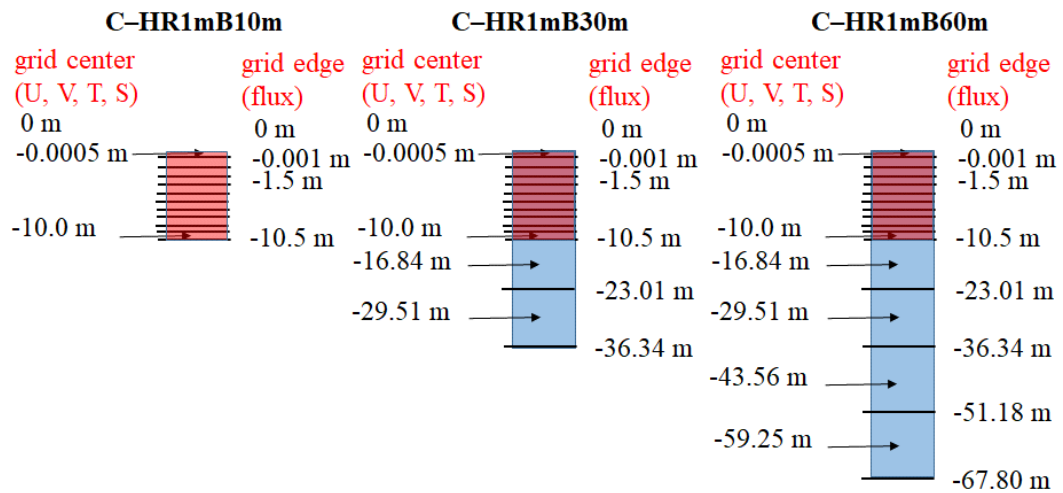
1251
1252   Figure A2. Diagrams showing the vertical grids in C–HR1mB10m, C–HR1mB30m and
1253   C–HR1mB60m. The model bottoms are 10, 30, and 60 m, respectively, unless the seabed
1254   is shallower than the above depth.
1255

Reference

Gaspar, P., Gregoris, Y., and Lefevre, J.-M.: A simple eddy kinetic energy model for simulations of the oceanic vertical mixing: tests at station papa and long-term upper ocean study site, J. Geophys. Res. -Oceans, 95, 16179–16193, https://doi.org/10.1029/JC095iC09p16179, 1990.

Grassl, H.: The dependence of the measured cool skin of the ocean on wind stress and total heat flux, Bounday-Layer Meteorol., 10, 465-474, https://doi.org/10.1007/BF00225865, 1976.

Hasse, L.: The sea surface temperature deviation and the heat flow at the sea–air interface, Bounday-Layer Meteorol., 1, 368-379, https://doi.org/10.1007/BF02186037, 1971.

Lan, Y.-Y., Tsuang, B.-J., Tu, C.-Y., Wu, T.-Y., Chen, Y.-L., and Hsieh, C.-I.: Observation and Simulation of Meteorology and Surface Energy Components over the South China Sea in Summers of 2004 and 2006, Terr. Atmos. Ocean. Sci., 21, 325–342, https://doi.org/ 10.3319/TAO.2009.04.07.01(A), 2010.

Mellor, G. L., and Yamada, T.: Development of a turbulence closure model for geophysical fluid problems, Rev. Geophys., 20, 851-875, https://doi.org/10.1029/RG020i004p00851, 1982.

Paulson, C. A. and Simpson, J. J.: The temperature difference across the cool skin of the ocean, J. Geophys. Res., 86, 11044-11054, https://doi.org/10.1029/JC086iC11p11044, 1981.

Tu, C.-Y., and Tsuang, B.-J.: Cool-skin simulation by a one-column ocean model, Geophys. Res. Lett., 32, L22602, https://doi.org/10.1029/2005GL024252, 2005.

Wu, J.: On the cool skin of the ocean, Boundary-Layer Meteorol., 31, 203-207, https://doi.org/10.1007/BF00121179, 1985.